CHAPTER-3

NON-LOCAL LINEAR STABILITY ANALYSIS OF SELF-GRAVITATING CHARGED DUST SPHERE

Abstract: *Application of local stability theory in self-gravitating astrophysical plasmas is indeed inadequate due to their non-uniform nature confirmed mainly by the differential scale-heights of the gravitationally stratified constituent species in establishing gravito-thermal equilibrium. We formulate exact non-local linear analysis for identifying the global gravito-electrostatic modes, discrete oscillations and associated instabilities in interstellar charged dust molecular cloud (DMC) sphere with mass-radius above the critical values. The realistic effects like equilibrium inhomogeneities, diverse gradient forces and dust flow-convection dynamics are included. The dispersion relations (eigenvalues) and amplitude-variations (eigenfunctions) are Fourier-methodologically derived, explored and analyzed. We see that the entire cloud supports spectrally heterogeneous mixture of the Jeans and electrostatic modes. It is shown that the lowest-order non-rigid diffused cloud surface boundary (CSB) is the most unstable interfacial layer due to enhanced coupling strength of bipolar electrostatic repulsion and unipolar self-gravitational attraction. Three distinct and spatio-spectrally isolated classes of global eigenmodes-dispersive, nondispersive and hybrid types-are identified and characterized together with prolific features. Dispersive features are found prominent in the ultra-high k-regime; whereas, non-dispersive characteristics in the ultra-low k-regime. Numerical illustrations demonstrate that the grain-charge plays destabilizing influential role for the electrostatic fluctuations, but stabilizing role for the self-gravitational counterparts. In contrast, the grain-mass plays stabilizing influence for the former, but destabilizing influence for the latter. The results can be useful to realize complex nonlocal astrophysical fluctuations from a new perspective of plasma-wall interaction philosophy.*

3.1 INTRODUCTION

Astrophysical dusty plasmas, which are the birth-sites of stars and other galactic objects, are indeed inhomogeneous in nature. Their inhomogeneous and non-uniform nature is evidenced mainly by the differential scale-heights of gravitationally stratified constituent species in establishing gravito-thermal equilibrium via plasma polarization (Coulomb separation, or sedimentation) in presence

of gravity [1-2]. An isolated isothermal gravitating dusty plasma gas or dust molecular cloud (DMC) in gravito-thermal equilibrium organizes itself in such a fashion that the heavier constituents (grains) preponderantly fill lower layers towards the central region of the total mass distribution, leaving the lighter species (electrons and ions) re-distributed in upper layers relative to the center. In the interstellar normal dusty plasma conditions [2], the grain-to-electron and grain-to-ion scale heights may, with all the pre-defined usual notations, be respectively compared as, $H_d/H_e \sim (m_d/m_i)(T_p/T_d) \sim 10^{13} >> 1$ and $H_d/H_i \sim (m_d/m_i)(T_p/T_d) \sim 10^{9} >> 1$. For a few km of scale-heights of the electrons and ions, the dust density scale-height may go a few parsec. It clearly indicates that a large-scale non-zero electrostatic potential is evolved in association with the gravity-induced stratification effects. Thus, gravity-induced ambipolar electrostatic space-charge polarization effects in the plasmas with large-scale non-zero equilibrium electric field giving large-scale plasma flow dynamics must be considered. This, in principle, implies that the existence of the gravity-induced non-zero electric field requires non-local analysis of waves, instabilities and fluctuations in inhomogeneous astrophysical dusty cloud environments. It may, however, be noted that the global or non-local collective plasma wave fluctuation dynamics in the complex astrophysical grainy cloud environments with the unipolar gravitationally-induced bipolar electrostatic polarization effects needed for maintaining the cloud equilibria taken into account has so far not been realized completely amid the non-uniform equilibrium points.

It may furthermore be pertinent to mention that contemplates of collective waves, oscillations and associated instabilities in ionized self-gravitating dusty plasmas (viz. dust molecular clouds, protostellar disks, interstellar and circumstellar clouds, etc.) are very essential due to their important role in the formation processes of stars, planets and other galactic elements [3-7]. The presence of inertially massive and electrically charged dust particulates make it more interesting to empathize the nascence mechanism of bounded astrophysical objects in the DMCs.

The interstellar dust mostly consists of Silicates ($(SiO_4)^{4-}$), Graphite (C), Amorphous Carbon (aC), Polycyclic Aromatic Hydrocarbon (PAH) molecules, Silicon Carbide (SiC), Magnesium Sulfide (MgS), Icy grain mantles composed of simple molecules (e.g., H_2O, NH_3, CH_3OH and CO), and organic refractory grain mantles rich in carbon and oxygen [7-9]. The grain morphologies are usually non-uniform in composition [7-9]. These are composed of heterogeneous multilayers of different constituents starting from the grain core to outer surface. The core is made up of silicates and carbon. The inner surface, just adjacent after the core, is formed with water and

ammonia at normal temperature (far below the plasma temperature); and the outer surface with oxygen, carbon monoxide and nitrogen [7-9]. The grain mass lies between ~10^{-9} - 10^{-21} kg with mass density $\rho_d = m_d n_d \sim 3\times10^{-21}$ kg m^{-3} in interstellar medium [4, 7, 9-10]. There are different classes of DMCs depending on their physical properties [11-13] as discussed elaborately in chapter 1. For example, they are Globular Clouds (GCs), Dark Clouds (DCs), Giant Molecular Clouds (GMCs), Dense Dust Clouds (DDCs), Diffuse Dust Molecular Clouds (DDMCs), Cirrus Clouds (CCs), and Supernova Remnant Clouds (SRCs), etc.

Star formation processes are governed by complex interplay between the gravitational attraction due to the massive grains; and agents such as, instability in the atmosphere, magnetic field, radiation and thermal pressure that resist compression. The supersonic turbulence and thermal instability lead to transient, dense clumpy structures. Some of the clumps begin to collapse under the condition that the gravitational force pulling inwards exceeds the gas pressure pushing outwards. Once the collapse starts, the process feeds on itself and makes it denser, and so on. Thus, the clumps fragment into many pieces. Fragmented pieces again continue to collapse on its own self-gravity until the gas temperature raises enough to balance gravitational effects. As a consequence of gravito-thermal balancing, it gives bounded structure in the form of protostars or pre-stellar cores [14]. The presence of flow and inhomogeneity is integral part. For example, interplay between self-gravity and flow can destabilize the dusty fluid, where both the electrostatic and Jeans instabilities may operate simultaneously. Jeans has predicted the instabilities of self-gravitating large gas clouds in the last century [15]. Chandrasekhar has worked on comparative investigation of the Jeans instability in self-gravitating fluids and plasmas; and has found that the hydrostatic gas pressure gradient and the Lorentz force stabilize the Jeans instability [16]. Pudritz has performed a local linear instability analysis of self-gravitating partially ionized magnetoplasma [17]. His main interesting result is that the fluctuation growth rate reduces to that of the Jeans instability for the large-wavelength limit with frictional modulation in the short-wavelength regime only. Recently, other authors have also studied local stabilities to explore the magnetic Jeans [5-6, 18-19] and tearing instabilities for understanding the involved fragmentation processes.

It is thus seen that, there might have been many earlier linear [5, 17, 20-22] and nonlinear [21, 23] stability analyses. Based on the reports, it is noted that the realistic DMC dynamics is indeed very complex to formulate. Equilibrium inhomogeneities and non-uniformities further complicate it. So, to the best of our knowledge, none has so far studied the nonlocal stability in

inhomogeneous and non-uniform configuration. In this chapter, we construct a theoretical methodological model for the same under spherical geometry.

In astrophysical berths, the grain dynamics is mainly controlled by gravitation; while, those of the electrons and ions are influenced overwhelmingly by electromagnetic counterparts. The two forces operate on two widely distinct scales. For micron and sub-micron sized grains, these forces become comparable, at least in principle, within an order of magnitude [20]. Our model is specially focused on the particular class of the DMCs, where the dust self-gravity is balanced by the force arising from shielded electric field on the charged dust [24]. The principal goal is centered on that the mass and scale-size of the cloud: greater than the Avinash-Shukla critical mass limit ($M_D > M_{AS} \sim 10^{18}$ kg) and critical scale length ($R_D > L_{AS} \sim 10^9$ m) for the maximum cloud mass. We apply nonlocal linear perturbation analysis around the inhomogeneous equilibrium. The derived eigenvalue and eigen-function equations are numerically illustrated. The unique characteristics found here are the excitation and evolution of new types of instabilities, which source to spatio-spectrally hybrid structures due to complex mode-mode coupling of the interplaying fluctuations.

3.2 PHYSICAL MODEL

A simplified field-free spherical self-gravitating charged DMC in astrophysical environment is considered in quasi-neutral hydrodynamic inhomogeneous equilibrium configuration. The plasma constituents are the thermal electrons, singly ionized positive ions and inertial spherical micron-sized dust grains of identical nature. The solid matter of the massive dust grains is embedded in the gaseous phase of the plasma on the Jeans scale. A bulk uniform flow is presumed to exist. On the Jeans scales of space and time, we neglect the inertia of the electrons and ions. The dust kinetic pressure, which is appropriate for the cloud of dimension much larger than the plasma Debye radius [24], is ignored. The dust charge is not constant, but taken as function of dust population density. It decreases with increase in dust density, and vice versa. The equilibrium electric field is finite non-zero arising due to gravity-induced electrostatic polarization effects of the plasma [1-2, 25]. The origin of such polarization lies in the mass-dependent gravitational stratification of the plasma constituents to establish reorganized gravito-thermal equilibrium. All other equilibrium characteristic features, as described by Avinash and Shukla, are retained without any loss of generality [24]. We consider that the total cloud mass contributed collectively by the heavier grains is greater than the Avinash–Shukla critical mass-size limiting values. The velocity convection

dynamics in the dust fluid is afresh included to see the real nature of the cloud modes globally.

3.3 BASIC GOVERNING EQUATIONS

The DMC model is figured as a quasi-static distribution of the multi-fluid constituent particles in hydrodynamic inhomogeneous equilibrium configuration. Avinash and Shukla have adopted such model to calculate critical mass-size limits for stable cloud structure [24], without dust velocity convection dynamics, governed by the following dynamical evolution equations. The electrons and ions with usual notations are respectively described by

$$qn_e\nabla\phi - \nabla p_e = 0, \text{ and} \tag{3.1}$$

$$-qn_i\nabla\phi - \nabla p_i = 0. \tag{3.2}$$

We apply the hydrodynamic model approximation (low-frequency), which enables us to assume the phase velocity $v_p = \omega/k$ of the fluctuations in the range $v_{te}, v_{ti} >> v_p >> v_{td}$; where v_{te}, v_{ti}, and v_{td} are thermal velocities of the electrons, ions and the charged grains, respectively. So, the electrons and ions are justifiably treated as the Boltzmannian particles (derivable from equations (3.1)-(3.2)). The dynamics of the dust fluid is collectively governed by

$$\frac{\partial n_d}{\partial t} + \nabla.\left(n_d \boldsymbol{v}_d\right) = 0, \text{ and} \tag{3.3}$$

$$\rho_d\left[\frac{\partial \boldsymbol{v}_d}{\partial t} + \left(\boldsymbol{v}_d.\nabla\right)\boldsymbol{v}_d\right] = -q_d n_d\nabla\phi - \rho_d\nabla\psi. \tag{3.4}$$

The system is closed by the coupling Poisson equations of the electrostatic and self-gravitational potential distributions, given respectively, as follows,

$$\nabla^2\phi = -4\pi\left[e\left(n_i - n_e\right) + q_d n_d\right], \text{ and} \tag{3.5}$$

$$\nabla^2\psi = 4\pi G\rho_d. \tag{3.6}$$

Here, n_e, n_i, and n_d are unnormalized electron (with charge "$-q$", temperature "T_e", and mass "m_e"), ion (with charge "q", temperature "T_e", and mass "m_i"), and dust (with charge "$q_d = -Z_d q$", temperature "T_d", and mass "m_d") number densities, respectively. The notations ϕ and ψ stand for unnormalized electrostatic and self-gravitational potentials, respectively. The dust flow velocity is designated by v_d. The electronic and ionic thermal pressures are dictated by their respective isothermal equations of state, $p_e = n_e T_e$ and $p_i = n_i T_i$, with temperature-scaling

$T_d << T_e \approx T_i = T$ (due to differential mass-scaling, $m_d >> m_i > m_e$). Lastly, $\rho_d = m_d n_d$ denotes the cloud mass density and $G = 6.67 \times 10^{-11}$ N m^2 kg^{-2} is the universal gravitational constant.

3.4 DERIVATION OF STABILITY MASS LIMIT

Avinash and Shukla have shown an upper limit of the total mass and scale extension of astrophysical dusty clouds for the stable configuration [24], as originally understood in case of the Chandrasekhar mass limit of compact astrophysical objects [16]. For the present DMC stability, we first derive its mass- and size-limits, in the light of our formalism, on the Jeans scale. This implies that if the mass and size are less than the Avinash-Shukla critical values, then the cloud is stable. In contrast, if it is greater than the critical values, the cloud becomes unstable and undergoes collapse self-gravitationally. The equation of force balance [24] for the charged dust fluid is,

$$\nabla p_e = -\rho_d \nabla \psi \,, \tag{3.7}$$

where, p_e is the electrostatic pressure (superscript '*e*' for 'electrostatic'). Now, spatially differentiating equation (3.7) and using equation (3.6), we get the Lane-Emden equation (LEE) on the self-gravitational pressure with spherical symmetry in the normalized form as follows,

$$\left(\frac{R_D}{\lambda_J}\right)^2 \left\{\frac{1}{\xi^2}\frac{\partial}{\partial \xi}\left(\frac{\xi^2}{\rho_D}\frac{\partial P_E}{\partial \xi}\right)\right\} = -\rho_D \tag{3.8}$$

Here, $R_D = R_{DMC} = \left(n_o T / 4\pi G m_d^2 n_{do}^2\right)^{1/2}$ is the DMC scale-size and λ_J is the Jeans length. Further, ξ is the radial distance normalized by the Jeans length λ_J, P_E is the electric pressure normalized by the plasma thermal pressure $P_{Eo} = n_o T$, and ρ_D is the cloud mass density normalized by equilibrium cloud mass density $\rho_{Do} = m_d n_{do}$.

It is seen that $R_D = 100\lambda_J$ m in the proposed model for $\lambda_J \sim 4.21 \times 10^9$ m, $m_d \sim 10^{-14}$ kg, $n_o / n_{do} \sim 10^4$, and $T \sim 1$ eV [4, 7, 09-10]. To derive the critical mass limit, the total mass [16, 24] of the DMC can analytically be calculated as,

$$M_D = \frac{TR_D^2}{Gm_d\lambda_J^2} I \,, \tag{3.9}$$

where, the integral $I = \int_0^{\xi} \rho_D r^2 dr \sim 1$, is a dimensionless number [24].

Now, from equation (3.9), we find that $M_D \sim 10^{21}$ kg. Avinash and Shukla have given the critical DMC mass limit as $M_{AS} \sim 10^{18}$ kg and critical length as $L_{AS} \sim 10^{9}$ m for equilibrium (stable) state [24]. In our model, the DMC mass ($M_D >> M_{AS}$) and scale-size ($R_D >> L_{AS}$) exceed the Avinash-Shukla critical values. Thus, by critical value estimation, the cloud model here is unstable and hence, interesting for global fluctuation analysis.

A schematic diagram of the considered dust cloud model is portrayed in figure 3.1. The fluctuating non-rigid surface well known to be located at $\xi = 3.5\lambda_J$ [26-27] is the lowest-order cloud surface boundary (CSB). The terminology 'lowest-order CSB', means the nearest concentric spherical electric potential surface boundary (formed by gravito-electrostatic balancing) relative to the cloud center. Thus, it is seen that the concentric surface located at $\xi = 6\lambda_J$ is the physical extension boundary of our stability, which corresponds to the unstable cloud size $R_D = 100\lambda_J$. For clarity, we re-state that $L_{AS} \sim 10^{9} \approx 2.37\times10^{-1}\lambda_J$, which indicates $\xi = 6\lambda_J \approx 25L_{AS}$. This justifies that the spherical cloud extension $\xi = 0\text{-}6\lambda_J$ $(> L_{AS})$, containing net mass $M \approx 25M_{AS}$ $(> M_{AS})$, is a good choice in physical parameter window for instability investigation in the considered cloud system.

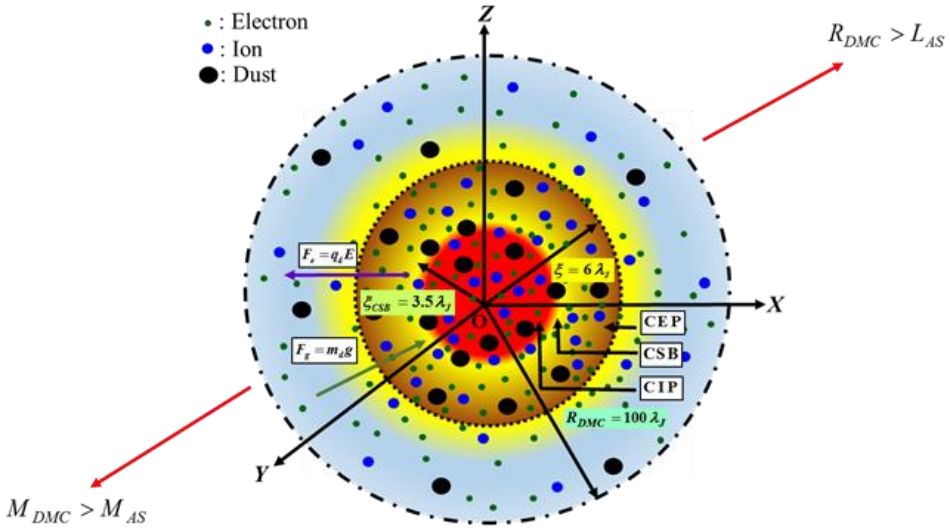

Figure 3.1 *Schematic diagram of the spherical DMC considered in the analysis. Various concentric spherical layers are described in the text.*

3.5 NON-LOCAL FLUCTUATION ANALYSIS

The normalized (by standard astrophysical parameters) form of equations (3.1)-(3.2) describing the electron and ion dynamics with spherically symmetric geometry are respectively as follows,

$$N_e \frac{\partial \theta}{\partial \xi} - \frac{\partial N_e}{\partial \xi} = 0, \text{ and} \tag{3.10}$$

$$N_i \frac{\partial \theta}{\partial \xi} + \frac{\partial N_i}{\partial \xi} = 0. \tag{3.11}$$

Integrating equations (3.10)-(3.11) spatially, we obtain the normalized Boltzmann distributions for the electrons and ions, respectively, as given below,

$$N_e = N_{eo} \exp(\theta), \text{ and} \tag{3.12}$$

$$N_i = N_{io} \exp(-\theta). \tag{3.13}$$

Similarly, the normalized forms of the evolution equations for dust grain dynamics in the fluid model approach are given below,

$$\frac{1}{M_d}\frac{\partial N_d}{\partial \tau} + N_d \frac{2}{\xi} + \frac{N_d}{M_d}\frac{\partial M_d}{\partial \xi} + \frac{\partial N_d}{\partial \xi} = 0, \text{ and} \tag{3.14}$$

$$\frac{\partial M_d}{\partial \tau} + M_d \frac{\partial M_d}{\partial \xi} = -\frac{q_d}{q}\frac{\partial \theta}{\partial \xi} - \frac{m_d}{q}\frac{\partial \eta}{\partial \xi}. \tag{3.15}$$

Again, the normalized closing form of the electrostatic and self-gravitational Poisson equations with spherical symmetry are respectively given by,

$$\frac{\partial^2 \theta}{\partial \xi^2} + \frac{2}{\xi}\frac{\partial \theta}{\partial \xi} = \left(\frac{\lambda_J}{\lambda_{De}}\right)^2 \left[N_e - N_i + Z_d N_d\right], \text{ and} \tag{3.16}$$

$$\frac{\partial^2 \eta}{\partial \xi^2} + \frac{2}{\xi}\frac{\partial \eta}{\partial \xi} = \left(\frac{\lambda_J}{\lambda_{De}}\right)^2 \frac{G m_d N_d}{q}. \tag{3.17}$$

The independent coordinates, like distance ξ and time τ, are normalized by the Jeans length λ_J and Jeans time ω_J^{-1} scales, respectively. Both the electrostatic potential θ and self-gravitational potential η are normalized by the same plasma thermal potential T/q, so as to compare fluctuation levels on common equivalent basis. N_e, N_i, and N_d are the concentrations of the electrons, ions, and grains normalized by the equilibrium plasma density n_o each. Moreover, M_d is the dust flow velocity normalized by the dust sound phase speed $C_{ss} = (T/m_d)^{1/2}$.

3.5.1 Electrostatic Fluctuations

We apply non-local linear perturbation on the relevant physical parameters as shown below,

$$\begin{bmatrix} N_e(\xi,\tau) \\ N_i(\xi,\tau) \\ N_d(\xi,\tau) \\ M_d(\xi,\tau) \\ \theta(\xi,\tau) \\ \eta(\xi,\tau) \end{bmatrix} = \begin{bmatrix} N_{eo}(\xi) \\ N_{io}(\xi) \\ N_{do}(\xi) \\ M_{do}(\xi) \\ \theta_o(\xi) \\ \eta_o(\xi) \end{bmatrix} + \begin{bmatrix} N_{e1}(\xi,\tau) \\ N_{i1}(\xi,\tau) \\ N_{d1}(\xi,\tau) \\ M_{d1}(\xi,\tau) \\ \theta_1(\xi,\tau) \\ \eta_1(\xi,\tau) \end{bmatrix}. \tag{3.18}$$

Here, we consider inhomogeneous equilibrium with gravity-induced polarization effects [1-2]. Using equation (3.18) to equations (3.12)-(3.17), we obtain linearized set of equations presented respectively as follows,

$$N_{e1}(\xi,\tau) = N_{eo}(\xi) exp\{\theta_o(\xi)\}\theta_1(\xi,\tau), \tag{3.19}$$

$$N_{i1}(\xi,\tau) = -N_{io}(\xi) exp\{-\theta_o(\xi)\}\theta_1(\xi,\tau), \tag{3.20}$$

$$\begin{aligned} &\frac{\partial N_{d1}(\xi,\tau)}{\partial \tau} + N_{d1}(\xi,\tau)\frac{\partial M_{do}(\xi)}{\partial \xi} + N_{do}(\xi)\frac{\partial M_{d1}(\xi,\tau)}{\partial \xi} + M_{d1}(\xi,\tau)\frac{\partial N_{do}(\xi)}{\partial \xi} \\ &+ M_{do}(\xi)\frac{\partial N_{d1}(\xi,\tau)}{\partial \xi} + \{M_{do}(\xi)N_{d1}(\xi,\tau) + N_{do}(\xi)M_{d1}(\xi,\tau)\}\frac{2}{\xi} = 0, \end{aligned} \tag{3.21}$$

$$\frac{\partial M_{d1}(\xi,\tau)}{\partial \tau} + M_{d1}(\xi,\tau)\frac{\partial M_{do}(\xi)}{\partial \xi} + M_{do}(\xi)\frac{\partial M_{d1}(\xi,\tau)}{\partial \xi} + \frac{q_d}{q}\frac{\partial \theta_1(\xi,\tau)}{\partial \xi} + \frac{m_d}{q}\frac{\partial \eta_1(\xi,\tau)}{\partial \xi} = 0, \tag{3.22}$$

$$\frac{\partial^2 \theta_1(\xi,\tau)}{\partial \xi^2} + \frac{2}{\xi}\frac{\partial \theta_1(\xi,\tau)}{\partial \xi} = \left(\frac{\lambda_J}{\lambda_{De}}\right)^2 \left[N_{e1}(\xi,\tau) - N_{i1}(\xi,\tau) + Z_d N_{d1}(\xi,\tau)\right], \text{ and} \tag{3.23}$$

$$\frac{\partial^2 \eta_1(\xi,\tau)}{\partial \xi^2} + \frac{2}{\xi}\frac{\partial \eta_1(\xi,\tau)}{\partial \xi} = \left(\frac{\lambda_J}{\lambda_{De}}\right)^2 \frac{Gm_d}{q} N_{d1}(\xi,\tau). \tag{3.24}$$

As we are interested in nonlocal linear stability analysis, we apply the Fourier technique for a first-order inhomogeneous plane wave analysis over equations (3.19)-(3.24) as inhomogeneous planar (radial) fluctuations [28]-a natural justified choice to describe the fields in non-uniform media. Before preceding further, the following points on the plane wave analysis, both as a methodical theory and as a strategic tool, may be worth mentioning for the sake of readers. A plane harmonic wave may be assumed as a limiting structure of a spherical wave from a considerably distant source (idealistically, induced point-source, in pure electromagnetic sense); where, the spherical wave front becomes almost planar. Although, realistic astrophysical clouds are known to have finite extension, the assumption of perturbations propagating as plane wave is valid under the condition that the dust cloud is unbounded, expanded infinitely and boundary effects are not directly of any

great immensity for the phenomena happening in the bulk plasma system [29-30]. The plane wave approximation under spherical symmetry is a simpler way (than other existing analytical methods) of concentrating on only one dimension (radial) thereby enabling us for the structure solutions in which the other two dimensions (azimuthal and co-latitudinal) do not enter at all. Another advantage in the analysis of translationally invariant systems derives from the fact that the natural representation of the system physical variables is in terms of plane waves with canonically minimum reduced number of degrees of freedom. As a consequence, this simplicity translates into faster computer run times with less memory requirements for exact analysis of the considered problem. The name "plane wave" is appropriate because the field vectors in the wave have the same value everywhere on each plane of constant ξ, for any fixed time τ, such that ξ is typically greater than the size of wave-scale length. In a broader and stricter sense, a plane wave is a wave whose phase is the same over a plane normal to the direction of wave propagation, even if the strength of the wave varies within that plane. These planes propagate in the radial direction at constant phase velocity of the considered fluctuations. Even for non-homogeneous, but isotropic and slowly-varying plasma medium with trifling viscosity, such approximations indeed represent a good starting point to the actual solutions. Accordingly, the sinusoidal fluctuations in inhomogeneous equilibrium, propagating as inhomogeneous plane waves here, can be written as,

$$\left.\begin{aligned}
N_{e1}(\xi,\tau) &= \tilde{N}_{e1}(\xi)e^{-i\omega\tau+ik\xi},\\
N_{i1}(\xi,\tau) &= \tilde{N}_{i1}(\xi)e^{-i\omega\tau+ik\xi},\\
N_{d1}(\xi,\tau) &= \tilde{N}_{d1}(\xi)e^{-i\omega\tau+ik\xi},\\
M_{d1}(\xi,\tau) &= \tilde{M}_{d1}(\xi)e^{-i\omega\tau+ik\xi},\\
\theta_1(\xi,\tau) &= \tilde{\theta}_1(\xi)e^{-i\omega\tau+ik\xi}, \text{ and}\\
\eta_1(\xi,\tau) &= \tilde{\eta}_1(\xi)e^{-i\omega\tau+ik\xi}.
\end{aligned}\right\} \qquad (3.25)$$

Here, ω is the fluctuation frequency normalized to the Jeans frequency $\omega_J\left(=\sqrt{4\pi G m_d n_{do}}\right)$ and k is the wave vector (angular wave number) normalized to the critical Jeans wave vector $k_J\left(=2\pi/\lambda_J\right)$. Now, applying equation (3.25) to equations (3.19)-(3.24), we get the equations as,

$$\tilde{N}_{e1}(\xi) = N_{eo}(\xi)exp\{\theta_o(\xi)\}\tilde{\theta}_1(\xi), \qquad (3.26)$$

$$\tilde{N}_{i1}(\xi) = -N_{io}(\xi) exp\{-\theta_o(\xi)\}\tilde{\theta}_1(\xi), \tag{3.27}$$

$$\left\{-i\Omega + \frac{\partial M_{do}(\xi)}{\partial \xi} + M_{do}(\xi)\left(\frac{\partial}{\partial \xi} + \frac{2}{\xi}\right)\right\}\tilde{N}_{d1}(\xi) + \left\{N_{do}(\xi)\left(\frac{\partial}{\partial \xi} + \frac{2}{\xi} + ik\right) + \frac{\partial N_{do}(\xi)}{\partial \xi}\right\}\tilde{M}_{d1}(\xi) = 0, \tag{3.28}$$

where, $\Omega = \{\omega - kM_{do}(\xi)\}$ is the Doppler-shifted frequency of the fluctuations.

$$\left\{-i\Omega + \frac{\partial M_{do}(\xi)}{\partial \xi} + M_{do}(\xi)\frac{\partial}{\partial \xi}\right\}\tilde{M}_{d1}(\xi) = -\frac{q_d}{q}\left(\frac{\partial}{\partial \xi} + ik\right)\tilde{\theta}_1(\xi) - \frac{m_d}{q}\left(\frac{\partial}{\partial \xi} + ik\right)\tilde{\eta}_1(\xi), \tag{3.29}$$

$$\frac{\partial^2 \tilde{\theta}_1(\xi)}{\partial \xi^2} + \left(\frac{2}{\xi} + 2ik\right)\frac{\partial \tilde{\theta}_1(\xi)}{\partial \xi} + \left(\frac{2ik}{\xi} - k^2\right)\tilde{\theta}_1(\xi)$$
$$= \left(\frac{\lambda_J}{\lambda_{De}}\right)^2\left[\tilde{N}_{e1}(\xi) - \tilde{N}_{i1}(\xi) + Z_d\,\tilde{N}_{d1}(\xi)\right] \quad \text{, and} \tag{3.30}$$

$$\frac{\partial^2 \tilde{\eta}_1(\xi)}{\partial \xi^2} + \left(\frac{2}{\xi} + 2ik\right)\frac{\partial \tilde{\eta}_1(\xi)}{\partial \xi} + \left(\frac{2ik}{\xi} - k^2\right)\tilde{\eta}_1(\xi) = \left(\frac{\lambda_J}{\lambda_{De}}\right)^2 \frac{Gm_d}{q}\,\tilde{N}_{d1}(\xi). \tag{3.31}$$

We solve equation (3.30) for $N_{d1}(\xi)$, $\partial/\partial\xi\{N_{d1}(\xi)\}$, $\partial^2/\partial\xi^2\{N_{d1}(\xi)\}$; equation (3.31) for $\eta_1(\xi)$; and use them in equations (3.28)-(3.29). After rigorous calculation and simplification with the assumption that $\{-i\Omega + \partial M_{do}(\xi)/\partial\xi + M_{do}(\xi)\partial/\partial\xi\}\tilde{M}_{d1}(\xi) \sim 0$ (valid for relatively massive stationary dust grains under cold-dust approximation), we get the nonlocal electrostatic eigen-function equation as set out below,

$$\frac{\partial^4 \tilde{\theta}_1(\xi)}{\partial \xi^4} + \left(\frac{\alpha_2}{\alpha_1}\right)\frac{\partial^3 \tilde{\theta}_1(\xi)}{\partial \xi^3} + \left(\frac{\alpha_3}{\alpha_1}\right)\frac{\partial^2 \tilde{\theta}_1(\xi)}{\partial \xi^2} + \left(\frac{\alpha_4}{\alpha_1}\right)\frac{\partial \tilde{\theta}_1(\xi)}{\partial \xi} + \left(\frac{\alpha_5}{\alpha_1}\right)\tilde{\theta}_1(\xi) = 0. \tag{3.32}$$

The various coefficients involved in equation (3.32) are expressed as given below,

$$\alpha_1 = \frac{M_{do}^2(\xi)}{Z_d}\left(\frac{\lambda_{De}}{\lambda_J}\right)^2, \tag{3.33}$$

$$\alpha_2 = \left(\frac{\lambda_{De}}{\lambda_J}\right)^2 \frac{1}{Z_d}\left\{M_{do}^2(\xi)\left(\frac{2}{\xi} + ik\right) + A_2\right\}, \tag{3.34}$$

$$\alpha_3 = \left(\frac{\lambda_{De}}{\lambda_J}\right)^2 \frac{1}{Z_d}\left[A_1 + A_2\left(\frac{2}{\xi} + ik\right) + M_{do}^2(\xi)\left\{\frac{2ik}{\xi} - k^2 - \frac{4}{\xi^2} - \left(\frac{\lambda_J}{\lambda_{De}}\right)^2\begin{pmatrix} N_{eo}(\xi)e^{\theta_o(\xi)} \\ + N_{io}(\xi)e^{-\theta_o(\xi)} \end{pmatrix}\right\}\right] -$$

$$\left(1+\frac{Gm_d^2}{Z_d q^2}\right)\left(\frac{2ik}{\xi}-k^2\right)^{-1}\left\{ik\frac{\partial N_{do}(\xi)}{\partial\xi}-k^2N_{do}(\xi)\right\}, \tag{3.35}$$

$$\alpha_4=\left(\frac{\lambda_{De}}{\lambda_J}\right)^2\frac{1}{Z_d}\left\{A_1\left(\frac{2}{\xi}+2ik\right)+A_2\left(\frac{2ik}{\xi}-k^2-\frac{2}{\xi^2}\right)+\frac{4M_{do}^2(\xi)}{\xi^3}\right\}-\frac{A_2}{Z_d}\begin{Bmatrix}N_{eo}(\xi)e^{\theta_o(\xi)}\\+N_{io}(\xi)e^{-\theta_o(\xi)}\end{Bmatrix}, \tag{3.36}$$
$$-\left(1+\frac{Gm_d^2}{Z_d q^2}\right)\left\{ik\frac{\partial N_{do}(\xi)}{\partial\xi}-k^2N_{do}(\xi)\right\}$$

$$\alpha_5=\frac{A_2}{Z_d}\frac{\partial}{\partial\xi}\left\{N_{eo}(\xi)e^{\theta_o(\xi)}+N_{io}(\xi)e^{-\theta_o(\xi)}\right\}-\frac{A_1}{Z_d}\left\{N_{eo}(\xi)e^{\theta_o(\xi)}+N_{io}(\xi)e^{-\theta_o(\xi)}\right\}+$$

$$\frac{M_{do}^2(\xi)}{Z_d}\frac{\partial^2}{\partial\xi^2}\left\{N_{eo}(\xi)e^{\theta_o(\xi)}+N_{io}(\xi)e^{-\theta_o(\xi)}\right\}+\left(\frac{\lambda_{De}}{\lambda_J}\right)^2\frac{1}{Z_d}\begin{Bmatrix}A_1\left(\frac{2ik}{\xi}-k^2\right)+\frac{2ikA_2}{\xi^2}-M_{do}^2(\xi)\\\frac{4ik}{\xi^3}\left(1+\left(\frac{\lambda_J}{\lambda_{De}}\right)^2\frac{Z_d^2N_{do}\xi^2}{2M_{do}^2(\xi)}\right)\end{Bmatrix}, \tag{3.37}$$

$$-\frac{q_d}{q}\left\{ik\frac{\partial N_{do}(\xi)}{\partial\xi}-k^2N_{do}(\xi)\right\}\left[1+\frac{m_d}{q}\left(\frac{2ik}{\xi}-k^2\right)^{-1}\begin{Bmatrix}\left(\frac{2ik}{\xi}-k^2\right)-\left(\frac{\lambda_J}{\lambda_{De}}\right)^2\\\left\{N_{eo}(\xi)e^{\theta_o(\xi)}+N_{io}(\xi)e^{-\theta_o(\xi)}\right\}\end{Bmatrix}\right]$$

$$A_1=-\Omega^2-2i\Omega\frac{\partial M_{do}(\xi)}{\partial\xi}+\left\{\frac{\partial M_{do}(\xi)}{\partial\xi}\right\}^2+M_{do}(\xi)\frac{\partial^2M_{do}(\xi)}{\partial\xi^2}+\left\{\frac{\partial M_{do}(\xi)}{\partial\xi}-i\Omega-\frac{M_{do}(\xi)}{\xi}\right\}M_{do}(\xi)\frac{2}{\xi}, \text{ and} \tag{3.38}$$

$$A_2=-2i\Omega M_{do}(\xi)\left(1-M_{do}(\xi)\frac{2}{\xi}\right)+3M_{do}(\xi)\frac{\partial M_{do}(\xi)}{\partial\xi}. \tag{3.39}$$

In the above equation, the term involving the lowest-order non-locality ($\partial^0/\partial\xi^0$) is the last term, where all other higher-order non-local terms would have been absent in case of local stability analysis. In all other remaining terms, different orders of non-locality appear in the form of different-order $\partial/\partial\xi$-operations. We equate the coefficient of the last term to derive the nonlocal dispersion relation of the fluctuations as,

$$\alpha_5=\frac{A_2}{Z_d}\frac{\partial}{\partial\xi}\left\{N_{eo}(\xi)e^{\theta_o(\xi)}+N_{io}(\xi)e^{-\theta_o(\xi)}\right\}-\frac{A_1}{Z_d}\left\{N_{eo}(\xi)e^{\theta_o(\xi)}+N_{io}(\xi)e^{-\theta_o(\xi)}\right\}+$$

$$\frac{M_{do}^2(\xi)}{Z_d}\frac{\partial^2}{\partial\xi^2}\left\{N_{eo}(\xi)e^{\theta_o(\xi)}+N_{io}(\xi)e^{-\theta_o(\xi)}\right\}+\left(\frac{\lambda_{De}}{\lambda_J}\right)^2\frac{1}{Z_d}\begin{Bmatrix}A_1\left(\frac{2ik}{\xi}-k^2\right)+\frac{2ikA_2}{\xi^2}-M_{do}^2(\xi)\\\frac{4ik}{\xi^3}\left(1+\left(\frac{\lambda_J}{\lambda_{De}}\right)^2\frac{Z_d^2N_{do}\xi^2}{2M_{do}^2(\xi)}\right)\end{Bmatrix}=0 \tag{3.40}$$

$$-\frac{q_d}{q}\left\{ik\frac{\partial N_{do}(\xi)}{\partial\xi}-k^2N_{do}(\xi)\right\}\left[1+\frac{m_d}{q}\left(\frac{2ik}{\xi}-k^2\right)^{-1}\begin{Bmatrix}\left(\frac{2ik}{\xi}-k^2\right)-\left(\frac{\lambda_J}{\lambda_{De}}\right)^2\\\left\{N_{eo}(\xi)e^{\theta_o(\xi)}+N_{io}(\xi)e^{-\theta_o(\xi)}\right\}\end{Bmatrix}\right]$$

The presence of equilibrium gradients in equation (3.40) reflects conversely that astrophysical plasma equilibria are indeed inhomogeneous and non-uniform in nature. Equation (3.40) gives the eigenvalue equation, which shows the nonlocal electrostatic fluctuations in simplified form as,

$$D_E(\omega,k) \equiv \omega^2 + E_1\omega + E_o = 0\,. \tag{3.41}$$

where,

$$E_o = kM_{do}(\xi)\left\{kM_{do}(\xi) - 2i\frac{\partial M_{do}(\xi)}{\partial\xi}\right\} - \left\{\frac{\partial M_{do}(\xi)}{\partial\xi}\right\}^2 - M_{do}(\xi)\frac{\partial^2 M_{do}(\xi)}{\partial\xi^2} +$$

$$M_{do}^2(\xi)\frac{2}{\xi}\left(\frac{1}{\xi} - ik\right) - \frac{2}{\xi}M_{do}(\xi)\frac{\partial M_{do}(\xi)}{\partial\xi} + \left(\frac{\lambda_J}{\lambda_{De}}\right)^2\frac{q_d Z_d}{q}\left\{ik\frac{\partial N_{do}(\xi)}{\partial\xi} - k^2 N_{do}(\xi)\right\}$$

$$\left\{1 + \frac{m_d}{q}\left(\frac{2ik}{\xi} - k^2\right)^{-1}\right\} + \left[\frac{2ik}{\xi} - k^2 - \left(\frac{\lambda_J}{\lambda_{De}}\right)^2\left\{N_{eo}(\xi)e^{\theta_o(\xi)} + N_{io}(\xi)e^{-\theta_o(\xi)}\right\}\right]^{-1}, \text{ and} \tag{3.42}$$

$$\left[\left\{-3\frac{\partial M_{do}(\xi)}{\partial\xi} - 2ikM_{do}(\xi) - M_{do}^2(\xi)\frac{2}{\xi}\right\}M_{do}(\xi)\left\{\frac{2ik}{\xi^2} + \left(\frac{\lambda_J}{\lambda_{De}}\right)^2\frac{\partial}{\partial\xi}\left\{\begin{matrix}N_{eo}(\xi)e^{\theta_o(\xi)} + \\ N_{io}(\xi)e^{-\theta_o(\xi)}\end{matrix}\right\}\right\}\right.$$

$$\left. + M_{do}^2(\xi)\left\{\frac{4ik}{\xi^3}\left(1 + \left(\frac{\lambda_J}{\lambda_{De}}\right)^2\frac{Z_d^2 N_{do}\xi^2}{2M_{do}^2(\xi)}\right) - \left(\frac{\lambda_J}{\lambda_{De}}\right)^2\frac{\partial^2}{\partial\xi^2}\left\{N_{eo}(\xi)e^{\theta_o(\xi)} + N_{io}(\xi)e^{-\theta_o(\xi)}\right\}\right\}\right]$$

$$E_1 = 2i\frac{\partial M_{do}(\xi)}{\partial\xi} - 2M_{do}(\xi)\left(k - \frac{i}{\xi}\right) + \left[\frac{2ik}{\xi} - k^2 - \left(\frac{\lambda_J}{\lambda_{De}}\right)^2\left\{N_{eo}(\xi)e^{\theta_o(\xi)} + N_{io}(\xi)e^{-\theta_o(\xi)}\right\}\right]^{-1} \tag{3.43}$$

$$2iM_{do}(\xi)\left[\frac{2ik}{\xi} + \left(\frac{\lambda_J}{\lambda_{De}}\right)^2\frac{\partial}{\partial\xi}\left\{N_{eo}(\xi)e^{\theta_o(\xi)} + N_{io}(\xi)e^{-\theta_o(\xi)}\right\}\right].$$

In case of infinite degree of spherical curvature $(\xi \to 0)$, equations (3.42)-(3.43) get modified as,

$$\left.\begin{matrix}E_o \approx \infty\text{, and} \\ E_1 \approx \infty\,.\end{matrix}\right\} \tag{3.44}$$

Again, for zero-degree of spherical curvature $(\xi \to \infty)$, equations (3.42)-(3.43) get reduced respectively to the forms as,

$$E_o \approx \left[kM_{do}(\xi)\left\{kM_{do}(\xi) - 2i\frac{\partial M_{do}(\xi)}{\partial\xi}\right\} - \left\{\frac{\partial M_{do}(\xi)}{\partial\xi}\right\}^2 - M_{do}(\xi)\frac{\partial^2 M_{do}(\xi)}{\partial\xi^2}\right]_{\xi=\infty} + \left(\frac{\lambda_J}{\lambda_{De}}\right)^2$$

$$\frac{q_d Z_d}{q}\left[ik\frac{\partial N_{do}(\xi)}{\partial\xi} - k^2 N_{do}(\xi)\right]_{\xi=\infty}\left(1 + \frac{m_d}{qk^2}\right) - \left[k^2 + \left(\frac{\lambda_J}{\lambda_{De}}\right)^2\left\{\begin{matrix}N_{eo}(\xi)e^{\theta_o(\xi)} + \\ N_{io}(\xi)e^{-\theta_o(\xi)}\end{matrix}\right\}_{\xi=\infty}\right]^{-1}$$

$$\left[\begin{array}{l}\left\{-3M_{do}(\xi)\frac{\partial M_{do}(\xi)}{\partial\xi}-2ikM_{do}^{2}(\xi)\right\}\left\{\left(\frac{\lambda_J}{\lambda_{De}}\right)^{2}\frac{\partial}{\partial\xi}\left\{\begin{array}{l}N_{eo}(\xi)e^{\theta_o(\xi)}+\\N_{io}(\xi)e^{-\theta_o(\xi)}\end{array}\right\}\right\}\\-M_{do}^{2}(\xi)\left\{\left(\frac{\lambda_J}{\lambda_{De}}\right)^{2}\frac{\partial^{2}}{\partial\xi^{2}}\left\{N_{eo}(\xi)e^{\theta_o(\xi)}+N_{io}(\xi)e^{-\theta_o(\xi)}\right\}\right\}\end{array}\right]_{\xi=\infty}, \text{ and} \tag{3.45}$$

$$E_1\approx\left[2i\frac{\partial M_{do}(\xi)}{\partial\xi}-2kM_{do}(\xi)\right]_{\xi=\infty}-2i\left[M_{do}(\xi)\right]_{\xi=\infty}\left[k^{2}+\left(\frac{\lambda_J}{\lambda_{De}}\right)^{2}\left\{\begin{array}{l}N_{eo}(\xi)e^{\theta_o(\xi)}\\+N_{io}(\xi)e^{-\theta_o(\xi)}\end{array}\right\}_{\xi=\infty}\right]^{-1} \tag{3.46}$$
$$\left(\frac{\lambda_J}{\lambda_{De}}\right)^{2}\left[\frac{\partial}{\partial\xi}\left\{N_{eo}(\xi)e^{\theta_o(\xi)}+N_{io}(\xi)e^{-\theta_o(\xi)}\right\}\right]_{\xi=\infty}.$$

Now, the following special cases may be worth explaining. In the Jeans limit of the fluctuations $(k\to 0)$, the coefficients of equation (3.41) get modified to the following respective forms,

$$E_o\approx-\left\{\frac{\partial M_{do}(\xi)}{\partial\xi}\right\}^{2}+M_{do}^{2}(\xi)\frac{2}{\xi^{2}}\left(1-\frac{\xi}{M_{do}(\xi)}\frac{\partial M_{do}(\xi)}{\partial\xi}\right)+\left\{N_{eo}(\xi)e^{\theta_o(\xi)}+N_{io}(\xi)e^{-\theta_o(\xi)}\right\}^{-1}$$
$$\left[\begin{array}{l}\left\{3M_{do}(\xi)\frac{\partial M_{do}(\xi)}{\partial\xi}+M_{do}^{2}(\xi)\frac{2}{\xi}\right\}\left\{\frac{\partial}{\partial\xi}\left\{N_{eo}(\xi)e^{\theta_o(\xi)}+N_{io}(\xi)e^{-\theta_o(\xi)}\right\}\right\}\\+M_{do}^{2}(\xi)\left\{\frac{\partial^{2}}{\partial\xi^{2}}\left\{N_{eo}(\xi)e^{\theta_o(\xi)}+N_{io}(\xi)e^{-\theta_o(\xi)}\right\}\right\}\end{array}\right]-M_{do}(\xi)\frac{\partial^{2}M_{do}(\xi)}{\partial\xi^{2}}, \text{ and} \tag{3.47}$$

$$E_1\approx 2i\frac{\partial M_{do}(\xi)}{\partial\xi}+i\frac{2}{\xi}M_{do}(\xi)-2iM_{do}(\xi)\left\{N_{eo}(\xi)e^{\theta_o(\xi)}+N_{io}(\xi)e^{-\theta_o(\xi)}\right\}^{-1}$$
$$\frac{\partial}{\partial\xi}\left\{N_{eo}(\xi)e^{\theta_o(\xi)}+N_{io}(\xi)e^{-\theta_o(\xi)}\right\}. \tag{3.48}$$

Again, in the electrostatic limit of the fluctuations $(k\to\infty)$, equations (3.42)-(3.43) get reduced to the following respective forms,

$$\left.\begin{array}{l}E_o\approx\infty, \text{ and}\\E_1\approx\infty.\end{array}\right\} \tag{3.49}$$

In case of homogeneous equilibrium configuration with M_{do}, $\theta_o=0$; N_{eo}, N_{io}, $N_{do}=1$, and $\partial/\partial\xi(N_{eo},N_{io},N_{do},M_{do},\theta_o)=0$, then equation (3.41) becomes,

$$\omega=\left\{\left(\frac{\lambda_J}{\lambda_{De}}\right)\left(\frac{Z_d q_d}{q}\right)^{1/2}\right\}k\left\{1-\frac{1}{k^{2}}\left(\frac{m_d}{q_d}\right)\left(1-\frac{2i}{k\xi}\right)^{-1}\right\}^{1/2}. \tag{3.50}$$

Now, using $\omega = \omega_r + i\omega_i$ to equation (3.50) and after simplification, we get,

$$\omega_r = \left\{\left(\frac{\lambda_J}{\lambda_{De}}\right)\left(\frac{Z_d q_d}{q}\right)^{1/2}\right\} k \left\{1 - \left(\frac{m_d}{2q_d}\right)\frac{1}{k^2}\right\}, \text{ and} \tag{3.51}$$

$$\omega_i = -\left\{\left(\frac{\lambda_J}{\lambda_{De}}\right)\left(\frac{Z_d q_d}{q}\right)^{1/2}\frac{m_d}{q_d}\right\}\frac{1}{k^2\xi}. \text{ and} \tag{3.52}$$

Here, it is observed from equation (3.51) that, the real part of frequency depends on the ratio of the Jeans-to-Debye lengths, wave vector, charge and mass of the grains. Likewise, it is seen from equation (3.52) that, the imaginary part of frequency depends on ratio of the Jeans-to-Debye lengths, charge and mass of the grains, wave vector and on the geometrical configuration as well. We can see that ω_i is a negative quantity, so the fluctuations should show damping behaviors. For infinite degree of curvature $(\xi \to 0)$, for a given k, one finds, $\omega_r = \omega_r$, and $\omega_i \to 0$. So, it is clear that, the damping or growth of the fluctuations depend on the cloud geometry. Again, for zero-degree curvature $(\xi \to \infty)$, $\omega_r = \omega_r$, and $|\omega_i| \to \infty$. Under such geometrical configurations, the fluctuations show infinite damping nature. In the Jeans limit $(k \to 0)$, one gets $\omega_r \to 0$, and $|\omega_i| \to \infty$. On the other hand, in the electrostatic limit $(k \to \infty)$, one finds $\omega_r \to \infty$, and $\omega_i \to 0$. In this limit, one can further see that $\omega_r \propto k$, which reveals purely acoustic behavior of the fluctuations. Now, the ratio between imaginary-to-real frequencies ($D_{P_E} = \omega_i/\omega_r$, or $G_{P_E} = \omega_i/\omega_r$), which is defined as damping (or, growth) rate per period [29] depending on the nature of the mode evolution, reads as,

$$D_{P_E} = \frac{2}{k\xi}\left\{1 + \left(\frac{2q_d}{m_d}\right)k^2\right\}. \tag{3.53}$$

For a given k, equation (3.53) further reduces to

$$D_{P_E} = \frac{\omega_i}{\omega_r} \propto \frac{1}{\xi}. \tag{3.54}$$

So, at $\xi, k \to 0$, one finds $D_{P_E} \to \infty$; and at $\xi, k \to \infty$, one sees $D_{P_E} \to 0$. So, in case of homogeneous equilibrium, it is observed that the damping rate per period is infinitely large at the

center, in the Jeans limit. The damping rate per period is zero for infinite distance, which corresponds to the electrostatic limit. The phase velocity and group velocity of the fluctuations in homogeneous equilibrium configuration are respectively given by,

$$V_{p_E} = \frac{\omega}{k} = \left\{\left(\frac{\lambda_J}{\lambda_{De}}\right)\left(\frac{Z_d q_d}{q}\right)^{1/2}\right\}\left\{1-\left(\frac{m_d}{2q_d}\right)\frac{1}{k^2}\right\}, \text{ and} \tag{3.55}$$

$$V_{g_E} = \frac{\partial\omega}{\partial k} = \left\{\left(\frac{\lambda_J}{\lambda_{De}}\right)\left(\frac{Z_d q_d}{q}\right)^{1/2}\right\}\left\{1+\left(\frac{m_d}{2q_d}\right)\frac{1}{k^2}\right\}. \tag{3.56}$$

Equations (3.55) and (3.56) reveal that the phase velocity and group velocity are inversely proportional to the wave vector. For a given k, $V_{P_E} \propto \left(-V_{g_E}\right)$, which shows that V_{P_E} and V_{g_E} are of opposite evolutionary phase. At $\xi \to 0, \infty$, we see that V_{P_E} and V_{g_E} remain unchanged. Again, at $k \to 0$, it is found that $\left|V_{P_E}\right|$, $V_{g_E} \to \infty$. As $k \to \infty$, we see that V_{P_E}, $V_{g_E} \to (\lambda_J/\lambda_{De})(Z_d q_d/q)^{1/2}$. Thus, in the Jeans limit, V_{P_E} and V_{g_E} are of infinite strength. In contrast, in the electrostatic limit, both are constant thereby revealing the acoustic-nature of the fluctuations. The phase dispersion and group dispersion [31-32] are given respectively as,

$$\Delta_{p_E} = \frac{\partial V_{p_E}}{\partial k} = \left\{\left(\frac{\lambda_J}{\lambda_{De}}\right)\left(\frac{m_d}{q_d}\right)\left(\frac{Z_d q_d}{q}\right)^{1/2}\right\}\frac{1}{k^3}, \text{ and} \tag{3.57}$$

$$\Delta_{g_E} = \frac{\partial V_{g_E}}{\partial k} = -\left\{\left(\frac{\lambda_J}{\lambda_{De}}\right)\left(\frac{m_d}{q_d}\right)\left(\frac{Z_d q_d}{q}\right)^{1/2}\right\}\frac{1}{k^3}. \tag{3.58}$$

Equations (3.57)-(3.58) show that $\Delta_{p_E} \propto \left(-\Delta_{g_E}\right) \propto k^{-3}$. Thus, the phase and group dispersions are of opposite evolutionary phase, each depending inversely upon the wave vector cubed. At, $\xi \to 0, \infty$; we see that Δ_{P_E}, Δ_{g_E} remain unchanged as V_{P_E} and V_{g_E}. Similarly, Δ_{P_E}, $\left|\Delta_{g_E}\right| \to \infty$, at $k \to 0,$ and Δ_{P_E}, $\Delta_{g_E} \to 0$, at $k \to \infty$ due to the non-dispersive nature of V_{P_E} and V_{g_E}.

3.5.2 Self-gravitational Fluctuations

To study the self-gravitational potential fluctuations of the unstable DMC globally, we derive self-gravitational eigen-function equation by using equations (3.25)-(3.31). In the derivation, we solve equation (3.31) for $N_{d1}(\xi)$, $\partial/\partial\xi\{N_{d1}(\xi)\}$, $\partial^2/\partial\xi^2\{N_{d1}(\xi)\}$, equation (3.30) for $\theta_1(\xi)$ and use them

in equations (3.28)-(3.29). After rigorous calculation with the assumption of $\tilde{M}_{d1}(\xi)\{-i\Omega+\partial M_{do}(\xi)/\partial\xi+M_{do}(\xi)\partial/\partial\xi\}\sim 0$ (valid for relatively massive stationary cold dust grains), we obtain the self-gravitational eigen-function equation as shown below,

$$\frac{\partial^4\tilde{\eta}_1(\xi)}{\partial\xi^4}+\left(\frac{\beta_2}{\beta_1}\right)\frac{\partial^3\tilde{\eta}_1(\xi)}{\partial\xi^3}+\left(\frac{\beta_3}{\beta_1}\right)\frac{\partial^2\tilde{\eta}_1(\xi)}{\partial\xi^2}+\left(\frac{\beta_4}{\beta_1}\right)\frac{\partial\tilde{\eta}_1(\xi)}{\partial\xi}+\left(\frac{\beta_5}{\beta_1}\right)\tilde{\eta}_1(\xi)=0\,. \tag{3.59}$$

where, the various coefficients in equation (3.59) are,

$$\beta_1=M_{do}^2(\xi)\,, \tag{3.60}$$

$$\beta_2=M_{do}^2(\xi)\left(\frac{2}{\xi}+2ik\right)+A_2\,, \tag{3.61}$$

$$\beta_3=A_1+\left(\frac{2}{\xi}+2ik\right)A_2+\frac{2M_{do}^2(\xi)k}{\xi}\left(i-\frac{2i}{\xi}-\frac{2}{\xi^2k}\right)-\left(\frac{\lambda_J}{\lambda_{De}}\right)^2\left\{ik\frac{\partial N_{do}(\xi)}{\partial\xi}-k^2N_{do}(\xi)\right\}$$
$$\frac{Gm_d^2q_d}{q^2}\left[\left(\frac{2ik}{\xi}-k^2\right)-\left(\frac{\lambda_J}{\lambda_{De}}\right)^2\left\{N_{eo}(\xi)e^{\theta_o(\xi)}+N_{io}(\xi)e^{-\theta_o(\xi)}\right\}\right]^{-1}\left(\frac{Z_dq}{Gm_d}+\frac{m_d}{q}\right)\,, \tag{3.62}$$

$$\beta_4=A_1\left(\frac{2}{\xi}+2ik\right)+\left(\frac{2ik}{\xi}-\frac{2}{\xi^2}-k^2\right)A_2+M_{do}^2\left(\frac{4}{\xi^3}-\frac{4ik}{\xi^2}\right)-\left(\frac{\lambda_J}{\lambda_{De}}\right)^2\left\{\begin{matrix}ik\dfrac{\partial N_{do}(\xi)}{\partial\xi}-\\ k^2N_{do}(\xi)\end{matrix}\right\}$$
$$\frac{Gm_d^2q_d}{q^2}\left(\frac{2}{\xi}+2ik\right)\left[\left(\frac{2ik}{\xi}-k^2\right)-\left(\frac{\lambda_J}{\lambda_{De}}\right)^2\left\{N_{eo}(\xi)e^{\theta_o(\xi)}+N_{io}(\xi)e^{-\theta_o(\xi)}\right\}\right]^{-1}\left(\frac{Z_dq}{Gm_d}+\frac{m_d}{q}\right), \text{ and} \tag{3.63}$$

$$\beta_5=A_1\left(\frac{2ik}{\xi}-k^2\right)-\frac{2ik}{\xi^2}A_2+M_{do}^2\,\frac{4ik}{\xi^3}-\left(\frac{\lambda_J}{\lambda_{De}}\right)^2\left\{\begin{matrix}ik\dfrac{\partial N_{do}(\xi)}{\partial\xi}-\\ k^2N_{do}(\xi)\end{matrix}\right\}\frac{Gm_d^2}{q^2}\left(\frac{2}{\xi}+2ik\right)$$
$$\left[1+\frac{Z_d\,q_d\,q}{Gm_d}\left(\frac{2ik}{\xi}-k^2\right)\left[\left(\frac{2ik}{\xi}-k^2\right)-\left(\frac{\lambda_J}{\lambda_{De}}\right)^2\left\{N_{eo}(\xi)e^{\theta_o(\xi)}+N_{io}(\xi)e^{-\theta_o(\xi)}\right\}\right]^{-1}\right]\,. \tag{3.64}$$

Similar to the electrostatic counterpart, we equate the coefficient of the lowest-order non-locality term in equation (3.59) to zero to get the eigenvalue equation as follows,

$$D_S(\omega,k)\equiv\omega^2+S_1\omega+S_o=0\,, \tag{3.65}$$

where,

$$S_o = \left[\begin{array}{l} \dfrac{2ik}{\xi^2}\left\{2ikM_{do}^2(\xi)+3M_{do}(\xi)\dfrac{\partial M_{do}(\xi)}{\partial\xi}\right\}+\left(\dfrac{\lambda_J}{\lambda_{De}}\right)^2\left\{\begin{array}{l} ik\dfrac{\partial N_{do}(\xi)}{\partial\xi}-k^2N_{do}(\xi) \\ +ikN_{do}(\xi)\dfrac{2}{\xi}\end{array}\right\}\dfrac{Gm_d^2}{q^2} \\ \left[1+\dfrac{Z_d\,q_d\,q}{Gm_d}\left(\dfrac{2ik}{\xi}-k^2\right)\left[\left(\dfrac{2ik}{\xi}-k^2\right)-\left(\dfrac{\lambda_J}{\lambda_{De}}\right)^2\left\{N_{eo}(\xi)e^{\theta_o(\xi)}+N_{io}(\xi)e^{-\theta_o(\xi)}\right\}\right]^{-1}\right] \end{array} \right]$$

$$M_{do}(\xi)\left\{k^2M_{do}(\xi)-\frac{\partial^2M_{do}(\xi)}{\partial\xi^2}-\frac{2}{\xi}\left(\frac{\partial M_{do}(\xi)}{\partial\xi}+\left(ik-\frac{1}{\xi}\right)M_{do}(\xi)\right)\right\}-\frac{\partial M_{do}(\xi)}{\partial\xi} \quad \text{, and (3.66)}$$

$$\left\{2ikM_{do}(\xi)+\frac{\partial M_{do}(\xi)}{\partial\xi}\right\}-\left(k^2-\frac{2ik}{\xi}\right)^{-1}$$

$$S_1 = 2i\frac{\partial M_{do}(\xi)}{\partial\xi}-2kM_{do}(\xi)+\frac{2}{\xi}iM_{do}(\xi)-\left(k^2-\frac{2ik}{\xi}\right)^{-1}\frac{4M_{do}(\xi)k}{\xi^2}. \quad (3.67)$$

The coefficients of the nonlocal fluctuations given by equations (3.66)-(3.67), get modified in case of infinite degree of geometrical curvature $(\xi\to 0)$, as shown below,

$$\left.\begin{array}{l} S_o\approx\infty, \text{ and} \\ S_1\approx\infty. \end{array}\right\} \quad (3.68)$$

Again, for zero-degree of curvature $(\xi\to\infty)$, equations (3.66)-(3.67) become,

$$S_o \approx \left[M_{do}(\xi)\left\{k^2M_{do}(\xi)-\frac{\partial^2M_{do}(\xi)}{\partial\xi^2}\right\}-\frac{\partial M_{do}(\xi)}{\partial\xi}\left\{2ikM_{do}(\xi)+\frac{\partial M_{do}(\xi)}{\partial\xi}\right\}\right]_{\xi=\infty}-\left(\frac{\lambda_J}{\lambda_{De}}\right)^2$$

$$\left\{\frac{i}{k}\frac{\partial N_{do}(\xi)}{\partial\xi}-N_{do}(\xi)\right\}_{\xi=\infty}\frac{Gm_d^2}{q^2}\left[1+\frac{Z_d\,q_d\,q}{Gm_d}\left[1+\left(\frac{\lambda_J}{\lambda_{De}}\right)^2\frac{1}{k^2}\left\{\begin{array}{l} N_{eo}(\xi)e^{\theta_o(\xi)} \\ +N_{io}(\xi)e^{-\theta_o(\xi)}\end{array}\right\}_{\xi=\infty}\right]^{-1}\right] \quad \text{, and} \quad (3.69)$$

$$S_1 \approx 2i\left[\frac{\partial M_{do}(\xi)}{\partial\xi}\right]_{\xi=\infty}-2k\left[M_{do}(\xi)\right]_{\xi=\infty}. \quad (3.70)$$

In the Jeans limit $(k\to 0)$, equations (3.66)-(3.67) get reduced to the following forms,

$$S_o \approx -M_{do}(\xi)\left(\frac{\partial^2M_{do}(\xi)}{\partial\xi^2}-\frac{2}{\xi}\frac{\partial M_{do}(\xi)}{\partial\xi}+M_{do}(\xi)\frac{2}{\xi^2}\right)-\left\{\frac{\partial M_{do}(\xi)}{\partial\xi}\right\}^2 \text{, and} \quad (3.71)$$

$$S_1 \approx 2i\frac{\partial M_{do}(\xi)}{\partial\xi}+\frac{2}{\xi}iM_{do}(\xi). \quad (3.72)$$

Similarly, in the electrostatic limit $(k \to \infty)$, equations (3.66)-(3.67) get altered to the forms,

$$\left.\begin{array}{l} S_o \approx \infty, \text{ and} \\ S_1 \approx \infty. \end{array}\right\} \tag{3.73}$$

For homogeneous equilibrium with M_{do}, $\theta_o = 0$; N_{eo}, N_{io}, $N_{do} = 1$, and $\partial/\partial\xi(N_{eo}, N_{io}, N_{do}, M_{do}, \theta_o) = 0$, equation (3.65) becomes,

$$\omega = \left(\frac{\lambda_J}{\lambda_{De}}\right)^2 2m_d^{1/2} Z_d \left(\frac{1}{k}\right)\left(1 + \frac{2i}{k\xi}\right)^{1/2}. \tag{3.74}$$

Now, using $\omega = \omega_r + i\omega_i$ in equation (3.74) and after simplification, we get

$$\omega_r == \left\{\left(\frac{\lambda_J}{\lambda_{De}}\right)^2 2Z_d\, m_d^{1/2}\right\}\frac{1}{k}, \text{ and} \tag{3.75}$$

$$\omega_i == \left\{\left(\frac{\lambda_J}{\lambda_{De}}\right)^2 2Z_d\, m_d^{1/2}\right\}\frac{1}{k^2\xi}. \tag{3.76}$$

Thus, the real and imaginary parts of frequency depend on the ratio of the Jeans-to-Debye lengths, charge and mass of the grains, wave vector and geometrical configuration. For a given k, at $\xi \to 0$; one has $\omega_r = \omega_r$, $\omega_i \to \infty$. Again, at $\xi \to \infty$; we see that $\omega_r = \omega_r$, $\omega_i \to 0$. This reveals that near the center of the cloud, self-gravitational fluctuations have infinite growing character. Similar to the electrostatic analysis, at $k \to 0$; one gets $\omega_r, \omega_i \to \infty$. Also, at $k \to \infty$; one derives $\omega_r, \omega_i \to 0$. Now, damping (or, growth) rate per period (Carbonell et al. 2004) depending on the nature of the mode-evolution comes out as,

$$D_{P_G} = \frac{1}{k\xi}. \tag{3.77}$$

For a given k, the damping rate per period given by equation (3.77) becomes

$$D_{P_G} = \frac{\omega_i}{\omega_r} \propto \left(\frac{1}{\xi}\right). \tag{3.78}$$

So, when $\xi,\ k \to 0$, $D_{P_G} \to \infty$; and $\xi,\ k \to \infty$, $D_{P_G} \to 0$. Thus, in case of homogeneous equilibrium, it is observed that both at the center and in the large-wavelength regime, the damping rate per period is infinitely large. At infinite distance and in the small-wavelength regime, the damping rate per period is zero. The phase velocity and group velocity of the fluctuations under homogeneous equilibrium configuration are derived as,

$$V_{p_G} = \frac{\omega}{k} = \left\{\left(\frac{\lambda_J}{\lambda_{De}}\right)^2 2Z_d\, m_d^{1/2}\right\}\frac{1}{k^2}, \text{ and} \tag{3.79}$$

$$V_{g_G} = \frac{\partial\omega}{\partial k} = \left\{\left(\frac{\lambda_J}{\lambda_{De}}\right)^2 2Z_d\, m_d^{1/2}\right\}\left(-\frac{1}{k^2}\right). \tag{3.80}$$

The relationship between the phase velocity and group velocity now goes as $V_{p_G} = -V_{g_G}$. Thus, for homogeneous equilibrium without any Jeans swindle, $V_{P_G} \propto \left(-V_{g_G}\right)$, which reveals that V_{P_G} and V_{g_G} propagate in opposite phase . Further, we see that, at $k \to 0$, both V_{P_G}, $V_{g_G} \to \infty$; and at $k \to \infty$, both V_{P_G}, $V_{g_G} \to 0$. This implies that, in the small-wavelength regime, no self-gravitational fluctuations propagate. It may be noted that V_{P_G}, and V_{g_G} are independent of geometrical effects. The corresponding phase dispersion and group dispersion [31-32] are now given by,

$$\Delta_{p_G} = \frac{\partial V_{p_G}}{\partial k} = \left\{\left(\frac{\lambda_J}{\lambda_{De}}\right)^2 4Z_d\, m_d^{1/2}\right\}\left(-\frac{1}{k^3}\right), \text{ and} \tag{3.81}$$

$$\Delta_{g_G} = \frac{\partial V_{g_G}}{\partial k} = \left\{\left(\frac{\lambda_J}{\lambda_{De}}\right)^2 4Z_d\, m_d^{1/2}\right\}\left(\frac{1}{k^3}\right). \tag{3.82}$$

From equations (3.81)-(3.82), we see that $\Delta_{pG} = \left(-\Delta_{gG}\right)\alpha\left(k^{-3}\right)$. Thus, Δ_{P_G}, and Δ_{g_G} are of opposite evolutionary phase and depend on wave vector. If $k \to 0$, we see that Δ_{P_G}, $\Delta_{g_G} \to \infty$; and at $k \to \infty$, one finds that Δ_{P_G}, $\Delta_{g_G} \to 0$, like V_{P_G} and V_{g_G}. It is interesting to note that Δ_{P_G}, and Δ_{g_G} are independent of any kind of geometrical influences.

5.6 RESULTS AND DISCUSSIONS

An evolutionary model to study the properties of global electro-gravitational modes in self-gravitating inhomogeneous interstellar DMC with all the characterizing equilibrium parameters varying radially is constructed under spherical symmetry. To study excitation and evolution of the fluctuations globally, we numerically integrate the electrostatic eigen-function equation [Eq. (3.32)] with suitable initial inputs by the fourth-order Runge–Kutta method [33]. Before presenting the numerical illustrations, different normalization constants are estimated methodologically from the judicious inputs available in the literature [4, 7, 9-10] as shown in Table 3.1.

Table 3.1: Normalization constants with estimated typical values

S. No	Physical property	Normalization constant	Typical value
1	Distance	Jeans length [λ_J]	4.21×10^{9} m
2	Time	Jeans time [ω_J^{-1}]	1.09×10^{12} s
3	Electrostatic potential	Plasma thermal potential [T/q]	1.00 V
4	Self-gravitational potential	Plasma thermal potential [T/q]	1.00 V
5	Population densities of electron, ion and grain	Equilibrium plasma population density [n_0]	1.00×10^{7} m^{-3}
6	Electric pressure	Plasma thermal pressure [n_0T]	1.47×10^{-12} N m^{-2}
7	Mass density	equilibrium mass density [$m_d n_{d0}$]	1.00×10^{-15} kg m^{-3}
8	Dust flow velocity	Dust sound phase speed [$C_{SS}=(T/m_d)^{1/2}$]	4.00×10^{-3} m s^{-1}

Figure 3.2 shows the profile of the normalized electrostatic potential fluctuations $\left(\tilde{\theta}_1(\xi)\right)$ with variation in normalized distance (ξ) and in normalized wave vector (k) of the fluctuations [by numerical integration of equation (3.32)]. Different initial values used are $(\theta)_i=-1.00\times10^{-2}$, $(\theta_\xi)_i=-1.00\times10^{-3}$, $(N_e)_i=9.50\times10^{-1}$, $(N_i)_i=9.00\times10^{-1}$, $(N_d)_i=1.00\times10^{-3}$, $(M_d)_i=1.01\times10^{-3}$, $(\eta)_i=-1.00\times10^{-5}$, $(\eta_\xi)_i=-1.29\times10^{-3}$, $(\theta_1)_i=-1.00\times10^{-8}$, $(\theta_{1\xi})_i=1.00\times10^{-4}$, $(\theta_{1\xi\xi})_i=-1.00\times10^{-7}$, and $(\theta_{1\xi\xi\xi})_i=-1.00\times10^{-9}$. The other input parameters kept constant are $m_d=2.50\times10^{-14}$ kg and $Z_d=1.00\times10^{2}$ [4, 7, 9-10]. The level of fluctuations is found maximum at 3.5 (on the Jeans scale), which is the lowest-order cloud surface boundary (CSB) [26-27]. The CSB act as an interfacial transition surface exhibiting bounded cloud interior plasma (CIP) dynamics on one hand, and unbounded cloud exterior plasma (CEP) dynamics on the other, as reported earlier in like situations [26-27]. On the exterior, the fluctuations show a damped periodic oscillatory behavior. The oscillatory behavior of the fluctuation indicates that the electro-gravitational interaction is not static, but dynamic in a periodic fashion via gravito-electrostatic interplay. The

periodic oscillations may be due to the compression of one species and rarefaction of the other, and vice versa, due to the dynamically periodic coupling processes. The damping nature in the CEP is attributable to the decrease in the coupling strength. In the *k*-space, no fluctuation propagates up to $k=1$ (which corresponds to $\lambda = 6.28\lambda_J$). This large-wavelength region is dominated by the self-gravitational fluctuations, as inertial dust grains are concentrated near the center. So, $k=1$ is behaving as a critical point for propagation of the fluctuations undergoing quasi-linear transformation into pure gravitational form. As *k* increases, the fluctuations grow linearly with a super-growth at $k=3.5$ ($\lambda = 1.79\lambda_J$). The growth occurs in the CIP due to the combined effect of the self-gravity, equilibrium inhomogeneities and gravity-induced plasma polarization. For $k>3.5$, the instability decays due to the gradually decreasing charge density in the CEP.

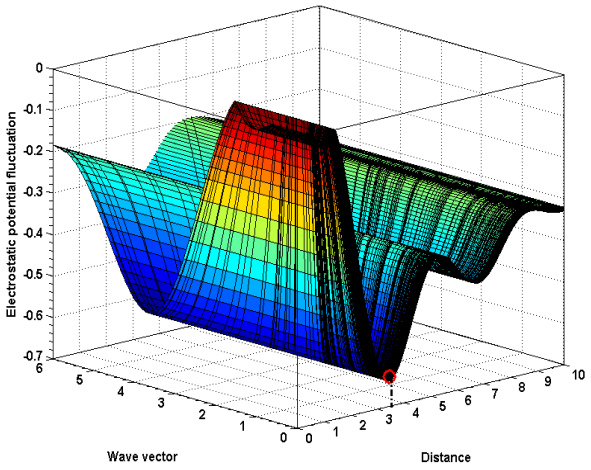

Figure 3.2 *Profile of the normalized electrostatic potential fluctuations* $\left(\tilde{\theta}_1(\xi)\right)$ *with variation in normalized distance* (ξ) *and in normalized wave vector* (k) *of the fluctuations. Various input and initial parameter values are given in the text.*

Figure 3.3 gives the profile of the normalized (a) real part of frequency, (b) imaginary part of frequency and (c) imaginary-to-real frequency ratio of the fluctuations with variation in normalized distance (ξ) and normalized wave vector (k). The different input initial values used are the same as figure 3.2. The real part (Figure 3.3(a)) is maximum at $\xi = 3.5$. This reveals that the CSB is the most unstable interfacial zone (as seen before in Figure 3.2). It decreases from the center to $\xi = 1.5$ outwards. This is due to the fact that the global mode-spectrum is dominated by the Jeans modes near the center. In the CEP, the real part of frequency gets damped out due to the

dispersive nature of the medium. The instability decays from the center with a super-decay at $k = 3$ ($\lambda = 2.09\lambda_J$), which coincides with the Jeans mode. After $k = 3$, the instability grows linearly with wave vector, which is the electrostatic acoustic mode-behavior. This linear growth of the global instability is due to the density inhomogeneity and gravity-induced polarization effects [1-2].

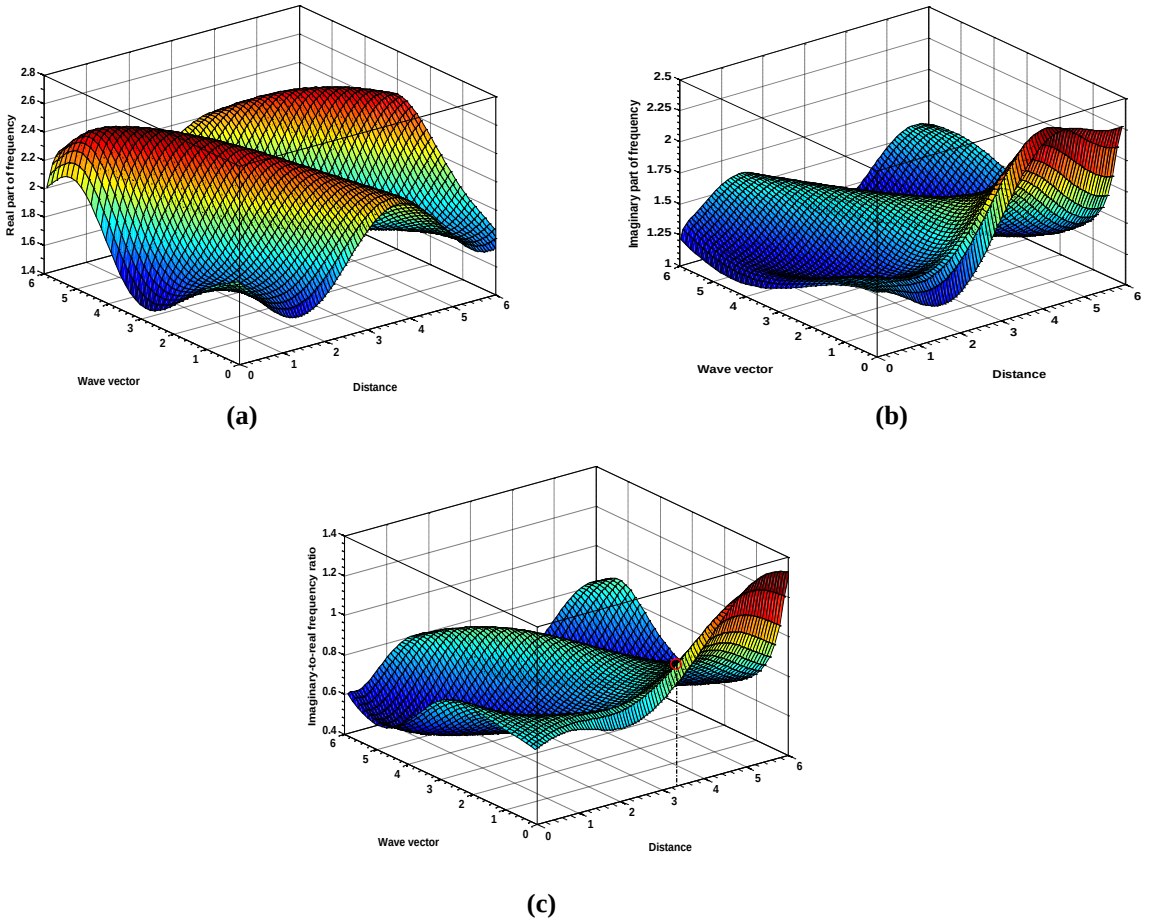

Figure 3.3 *Profile of the normalized (a) real part of frequency, (b) imaginary part of frequency, and (c) imaginary-to-real frequency ratio of the fluctuations with variation in normalized distance* (ξ) *and in normalized wave vector* (k). *Different input initial values used are the same as figure 3.2.*

In the long-wavelength region, the global instability behaves as the usual Jeans mode; and in the short-wavelength region, the Jeans mode is converted into acoustic mode via gravitational condensation of gravitational waves. So, the instability evolves as a hybrid structure due to mode-mode coupling of electro-gravitational fluctuations. The imaginary frequency part always shows growth, or damping rate of the fluctuations. It shows a three-scale behavior in the ξ – space (Figure

3.3(b)). The imaginary frequency decreases from the center to $\xi = 1.5$. After that, it increases linearly with a maximum and saturated value at $\xi = 4$ outwards. The instability is damped in the long-wavelength region with a super-decay at $k = 4$ ($\lambda = 1.57\lambda_J$) and it grows linearly in the short-wavelength region. Figure 3.3(c) shows the ratio of imaginary-to-real frequency. In the ξ – space, the ratio again shows three-scale behavior with a transition from slight damping-growth rate per period. The growth rate per period is 1 at $\xi = 3.5$. So, the linear theory is applicable for the study of stability of CIP and beyond the CSB the nonlinear theory has to be applied for the CEP stability. In the *k*-space, the frequency ratio grows linearly from the center and shows a super-growth at $k = 3$ ($\lambda = 2.09\lambda_J$). After the super-growth, there is a sharp damping with a super-decay at $k = 4$ ($\lambda = 1.57\lambda_J$) and then, it shows a linearly growing behavior.

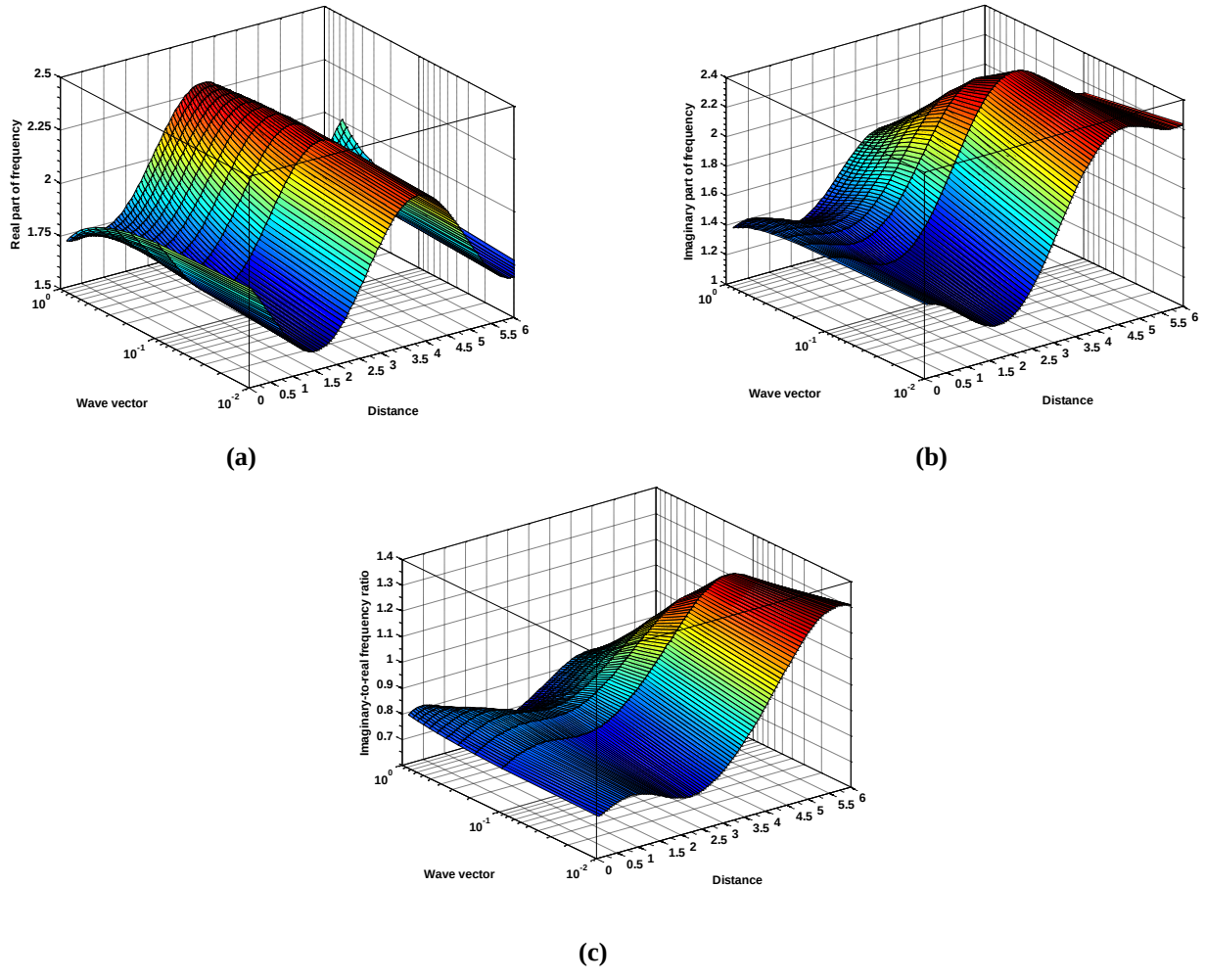

Figure 3.4 *Same as figure 3.3, but in the large-wavelength regime ($k \to 0$).*

Figure 3.4 shows the profiles same as figure 3.3, but in the large-wavelength regime ($k \to 0$). All the profiles in the ultra-low k limit show nondispersive nature of the fluctuations due to the Jeans instability, dominating in the large-wavelength regime.

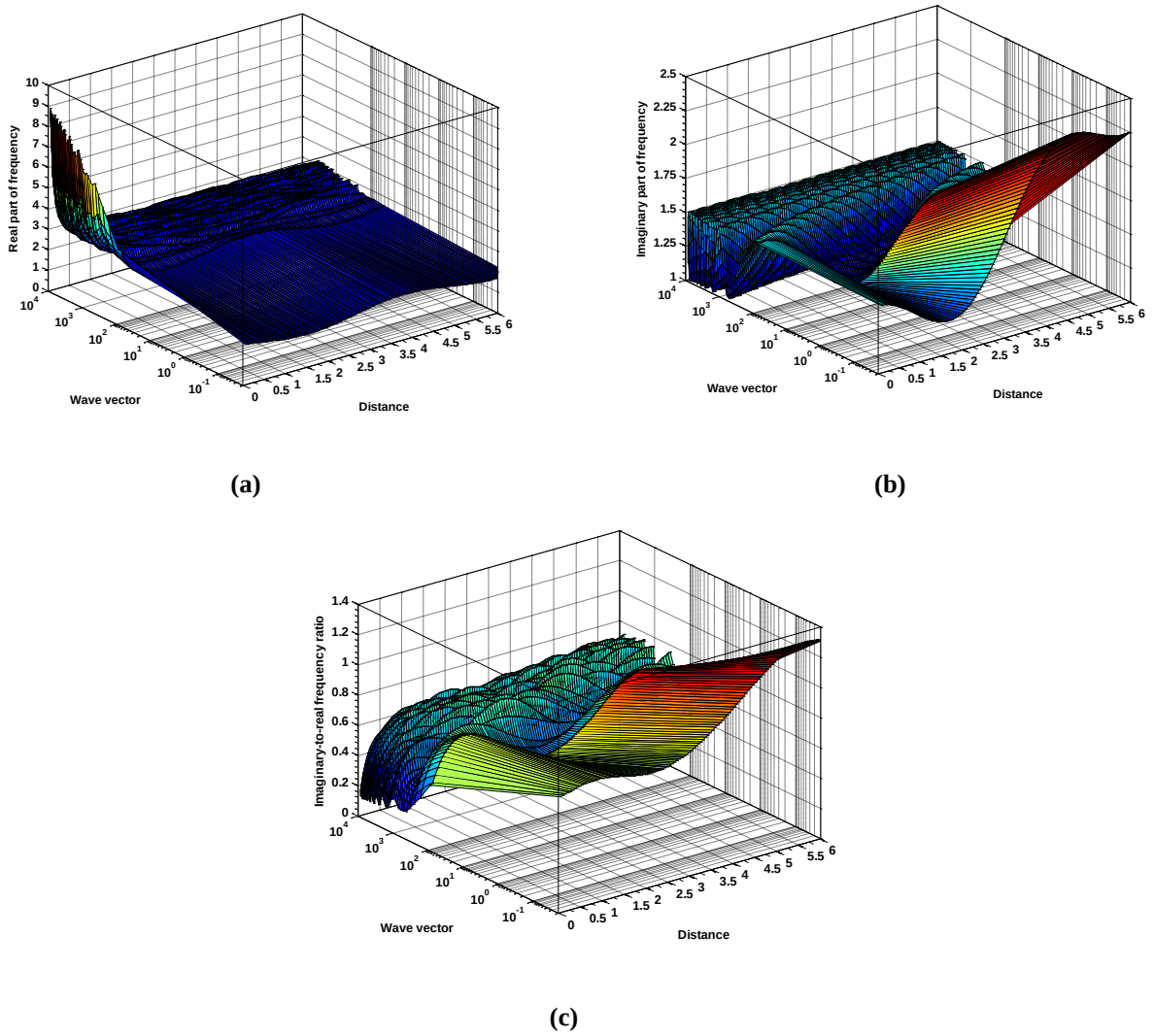

(a) **(b)**

(c)

Figure 3.5 *Same as figure 3.3, but in the small-wavelength regime ($k \to \infty$).*

Similarly, figure 3.5 shows the profiles in the small-wavelength regime ($k \to \infty$). In the ultra-high k limit, all the profiles show the dispersive characteristics of the fluctuations. The real part of frequency (Figure 3.5(a)) grows quasi-linearly with some background oscillations in the ultra-high k limit, which depicts the acoustic behavior. The imaginary part displays damping oscillatory behavior in the small-wavelength regime (Figure 3.5(b)). The ratio of imaginary-to-real frequency

signifies the damping nature of the instability in the ultra-high k limit (Figure 3.5(c)).

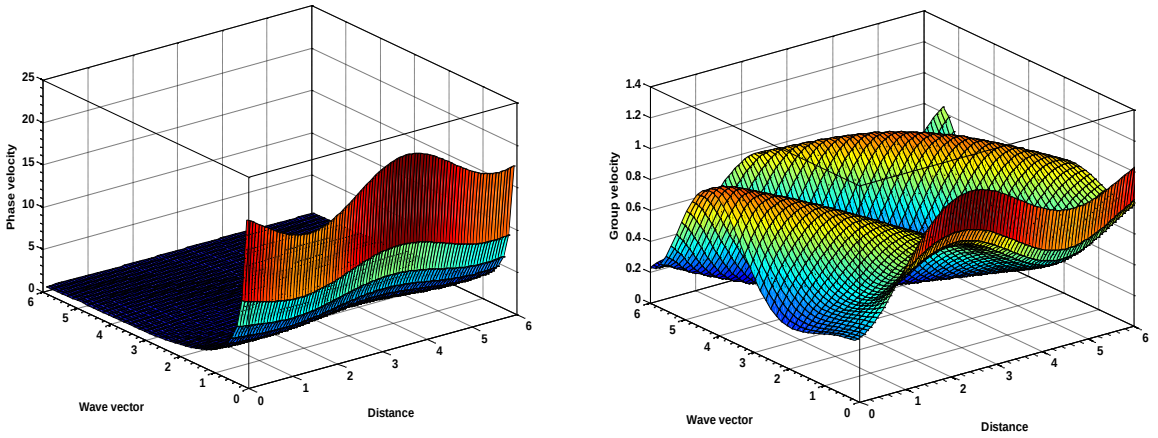

(a) **(b)**

Figure 3.6 *Profile of the normalized (a) phase velocity, and (b) group velocity of the fluctuations with variation in normalized distance* (ξ) *and in normalized wave vector* (k)*. The different input initial values used are the same as figure 3.2.*

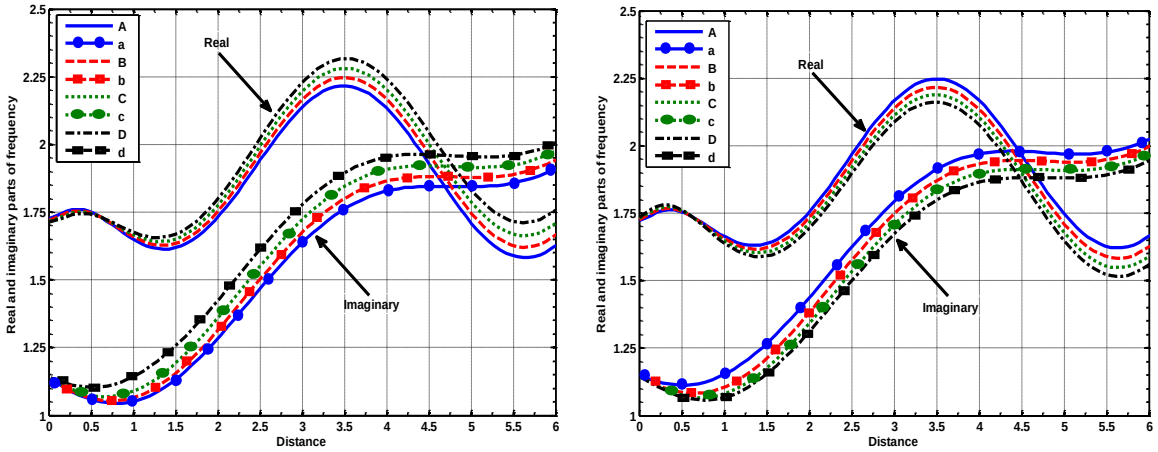

(a) **(b)**

Figure 3.7 *Spatial profile of the real part (A, B, C, D) and imaginary part (a, b, c, d) of the* $\theta(\xi)$*-fluctuation frequency with variation in (a)* Z_d *and (b)* m_d*, correspondingly, under the same condition as figure 3.2. Different lines in (a) correspond to* $Z_d = 100$ *(blue), 102 (red), 104 (green), and 106 (black), respectively. Again, different lines in (b) link to* $m_d = 2.49\times10^{-14}$ *(blue),* 2.50×10^{-14} *(red),* 2.51×10^{-14} *(green), and* 2.52×10^{-14} *kg (black), respectively.*

Figure 3.6 shows the profile constructs of the normalized (a) phase velocity and (b) group velocity of the fluctuations with variation in normalized distance (ξ) and in normalized wave vector (k). The different input initial values used are the same as figure 3.2. We see that the phase velocity decreases from the center up to $\xi = 1.5$ due to the strong self-gravitational attractive force sourced by the massive grains. In the ξ-region with $1.5 < \xi < 3.5$, the phase velocity increases linearly with the maximum value at $\xi = 3.5$, thereby showing the most unstable nature of the CSB. In the CEP, the phase velocity decreases due to the small drifting of charged species from the CIP to CEP. In the k-space, the phase velocity decays sharply from $k = 0$ to $k = 1.5$. For $k > 1.5$, it decays with very small gradient. Thus, the fluctuations are dispersive in nature with maximum dispersive behavior in the large-wavelength region ($k = 1.5$) due to strong self-gravitational effects. The velocity of the wave envelope is found to be maximum at $\xi = 3.5$ due to the most unstable nature of the CSB. The group velocity shows nonlinear behavior in the CEP, as the growth rate per period exceeds unity beyond the CSB. It is seen that the group velocity shows almost constant but with slight damping nature in the long-wavelength region due to strong self-gravity. In the regime $2.1 < k \leq 4.5$, the group velocity increases linearly with the maximum value at $k = 4.5$ ($\lambda = 1.39\lambda_J$). The velocity of the instability is damped out in the very short-wavelength regime ($k > 4.5$) due to very small drifting of the charged species in the CEP.

Figure 3.7 graphically displays the spatial profile of the real part (A, B, C, D) and imaginary part (a, b, c, d) (rescaled by dividing with 1.28) of the $\theta(\xi)$-fluctuation frequency with variation in (*a*) Z_d and (*b*) m_d, correspondingly, under the same condition as figure 3.2. Different lines in (*a*) correspond to $Z_d = 100$ (blue), 102 (red), 104 (green), and 106 (black), respectively. Again, different lines in (*b*) link to $m_d = 2.49 \times 10^{-14}$ kg (blue), 2.50×10^{-14} kg (red), 2.51×10^{-14} kg (green), and 2.52×10^{-14} kg (black), respectively. The real and imaginary parts of fluctuation frequency (Figure 3.7(a)) increases with increase in Z_d and decreases (Figure 3.7(b)) with increase in m_d. It may be noted that as Z_d increases, the electrostatic repulsive force increases. Hence, the growth rate increases. But, when m_d increases, the self-gravitational attractive force increases, which may dominate the fluctuation growth rate. As a result, the growth rate decreases. Thus, grain charge (Z_d) behaves as destabilizing source and grain mass (m_d) acts as a stabilizing source of the fluctuations. The observed features are in agreement with those obtained by others in the past

[34]. From figure 3.7(a), the value of real and imaginary parts at the CSB are $(\omega_r)_E$, $(\omega_i)_E$ ~ 2.25 each. Similarly, from figure 3.7(b), we get $(\omega_r)_E$, $(\omega_i)_E$ ~ 2.2 each at the CSB. It is found that, for both the cases (Figures 3.7(a)-3.7(b)), the real part shows constant value for $0 \le \xi \le 0.5\lambda_J$ and variation increases as frequency evolves away from $\xi = 0.5\lambda_J$.

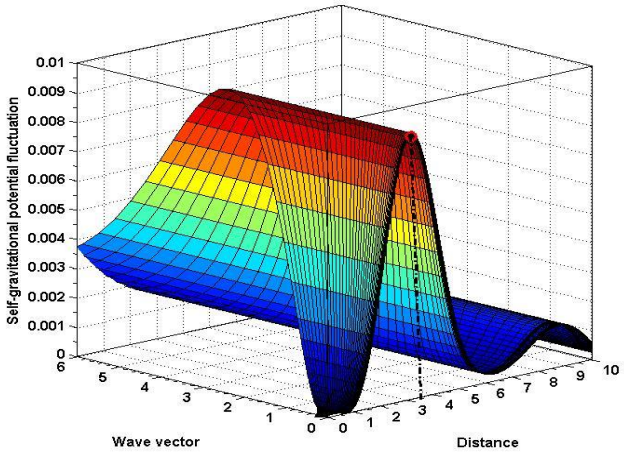

Figure 3.8 *Profile of the normalized self-gravitational potential fluctuations* $(\tilde{\eta}_1(\xi))$ *with normalized distance* (ξ) *and in normalized wave vector* (k) *of the fluctuations. Various input and initial parameter values are given in the text.*

Figure 3.8 gives the profile of the normalized self-gravitational potential fluctuations $(\tilde{\eta}_1(\xi))$with normalized distance (ξ) and normalized wave vector (k). Different initial values used here are $(\theta)_i = -1.00\times10^{-3}$, $(\theta_\xi)_i = -1.00\times10^{-4}$, $(N_e)_i = 8.10\times10^{-1}$, $(N_i)_i = 8.00\times10^{-1}$, $(N_d)_i = 1.00\times10^{-2}$, $(M_d)_i = 5.00\times10^{-3}$, $(\eta)_i = -1.00\times10^{-4}$, $(\eta_\xi)_i = -9.00\times10^{-2}$, $(\eta_1)_i = 1.00\times10^{-2}$, $(\eta_{1\xi})_i = -1.00\times10^{-5}$, $(\eta_{1\xi\xi})_i = -1.00\times10^{-9}$, and $(\eta_{1\xi\xi\xi})_i = -1.00\times10^{-10}$. The other input parameters kept constant are the same as in figure 3.2. It is interesting to see that the CSB is the most unstable interfacial zone, as the self-gravitational fluctuation is again the maximum at $\xi = 3.5$ like the electrostatic counterparts. The electrostatic and self-gravitational fluctuations evolve with opposite polarities due to the electro-gravitational coupling of the electrostatic repulsive and self-gravitational attractive effects. In the CEP, the self-gravitational fluctuations decrease due to decrease in dust density distribution as well as coupling between two counter-acting forces. The

self-gravitational fluctuations show a unique characteristic feature of almost zero-value from the center up to $\xi = 0.5$ and $k = 0.5$ in the CIP. The self-gravitational fluctuation grows linearly in the large-wavelength region ($0.5 < k \leq 2$) with a super-growth at $k = 2$ ($\lambda = 3.14\lambda_J$). For $k > 2$, the self-gravitational instability decays due to low-concentration of the massive grains in the CEP.

Figure 3.9 exhibits the profile of the normalized (a) real part of frequency, (b) imaginary part of frequency, (c) imaginary part of frequency with different orientation, and (d) imaginary-to-real frequency ratio of the fluctuations with normalized distance (ξ) and normalized wave vector (k). The different input initial values used are the same as in figure 3.8. The real part of frequency shows the maximum value at the center, and it decreases linearly with distance (Figure 3.9(a)). So, it is clear that near the center, the Jeans mode plays the dominating role due to the large-accumulation of the massive grains. In the k-space, the real frequency part shows a linearly damping characteristic feature from the center with a super-decay at $k = 2.5$ ($\lambda = 2.51\lambda_J$). From the super-decay point, the real part increases linearly with wave vector. The long-wavelength region, in which frequency profile shows damping behavior, is the Jeans mode-dominated region. Furthermore, the short-wavelength region, in which instability grows linearly, is the electrostatic mode-dominated region. Thus, a unique transition from the Jeans mode to electrostatic mode is found in the DMC (Figure 3.9(a)). So, the instability evolves as a hybrid structure due to intrinsic mode-mode coupling of electro-gravitational nature. The imaginary frequency profile shows the maximum value at $\xi = 3.5$, which re-confirms the most unstable nature of the CSB (Figure 3.9(b)). In the k-space, the imaginary part gradually grows with a super-growth value at $k = 3.7$ ($\lambda = 1.69\lambda_J$). Beyond it, the instability damps out. Figure 3.9(c) shows the imaginary frequency in different orientation to observe the evolution patterns more clearly. Figure 3.9(d) shows the profile of imaginary-to-real frequency ratio with variation in ξ and k. In the ξ-space, it again shows a transition from growth-to-damping rate per period. The growth rate per period is 1 at $\xi = 1.5$. So, the linear theory is applicable for $\xi \leq 1.5$. The growth rate is the maximum at $\xi = 3.5$, which again reveals the same on the CSB. Beyond the CSB, growth rate per period changes to damping rate per period. Thus, the self-gravitational fluctuations show damping behavior in the CEP due to the less dust concentration. In the k-space, the imaginary-to-real frequency ratio grows linearly from the center and shows a super-growth at $k = 3.4$ ($\lambda = 1.84\lambda_J$). So, in the long-wavelength region, the

Jeans mode plays the dominating role. Beyond the super-growth point, there is a sharp damping with a super-decay at $k = 6$ ($\lambda = 1.04\ \lambda_J$).

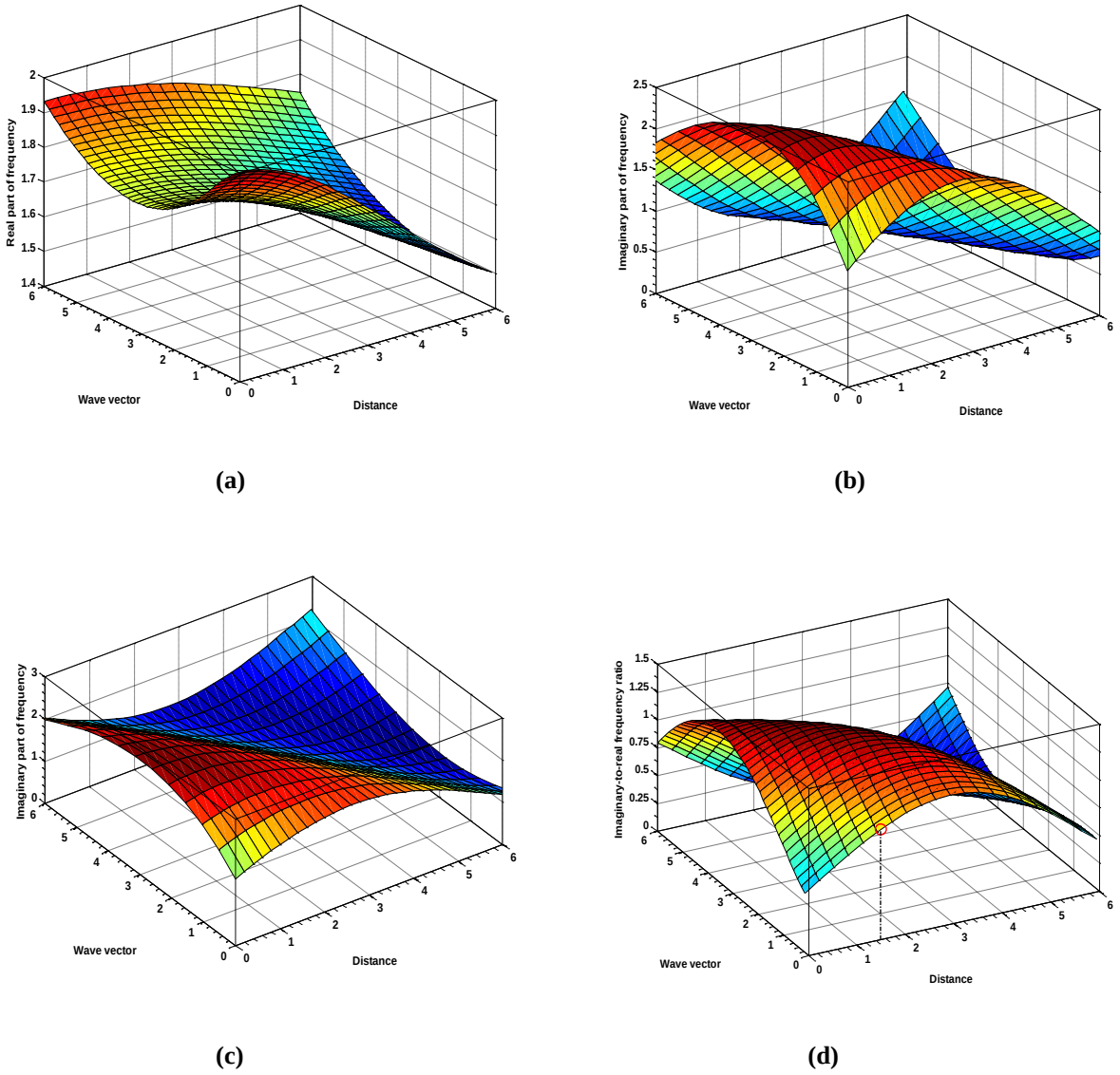

Figure 3.9 *Profile of the normalized (a) real part of frequency, (b) imaginary part of frequency, (c) imaginary part of frequency with different orientation, and (d) imaginary-to-real frequency ratio of the fluctuations with normalized distance* (ξ) *and in normalized wave vector* (k)*. The different input values used are the same as figure 3.8.*

Figure 3.10 shows the same as figure 3.9, but in the large-wavelength regime ($k \to 0$). All the profiles in the ultra-low k limit show dispersive nature. The imaginary part shows the growing

nature of the instability in the large-wavelength regime (Figure 3.10(b)). This observation reveals that that, the self-gravitational fluctuation instability, i.e., the Jeans instability grows in the large-wavelength regime.

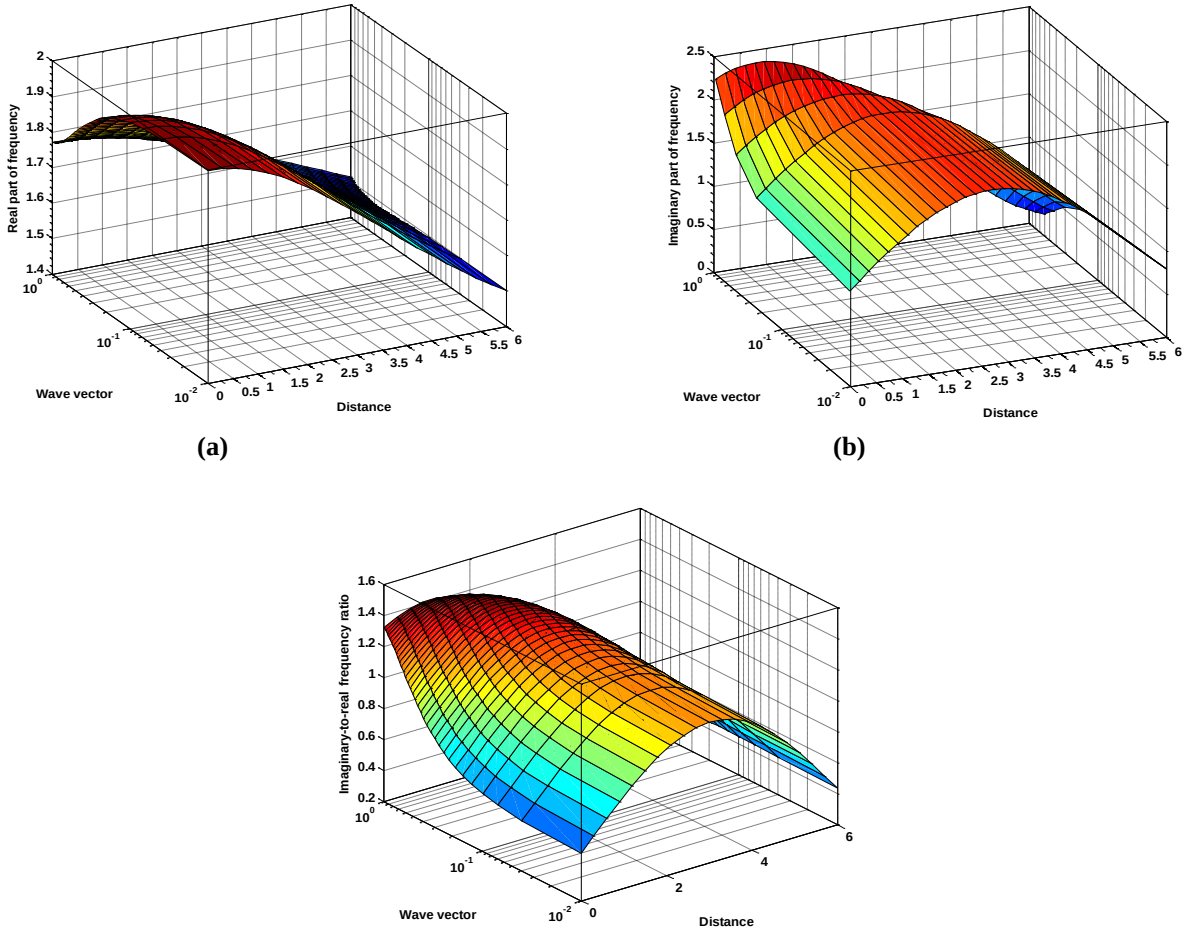

Figure 3.10 *Same as figure 3.9, but in the large-wavelength regime (*$k \to 0$*).*

Figure 3.11 shows the profile in the small-wavelength regime ($k \to \infty$) under the same condition as figure 3.9. In the ultra-high k limit, the real part shows hybrid characteristics of the instabilities with multiple transition from the Jeans to electrostatic modes (Figure 3.11(a)). In the extremely high-k limit, the instability behaves as purely acoustic-mode like the electrostatic counterpart. The imaginary part (Figure 3.11(b)) and imaginary-to-real frequency ratio (Figure 3.11(c)), in the ultra-high k limit show similar behaviors as the electrostatic ones.

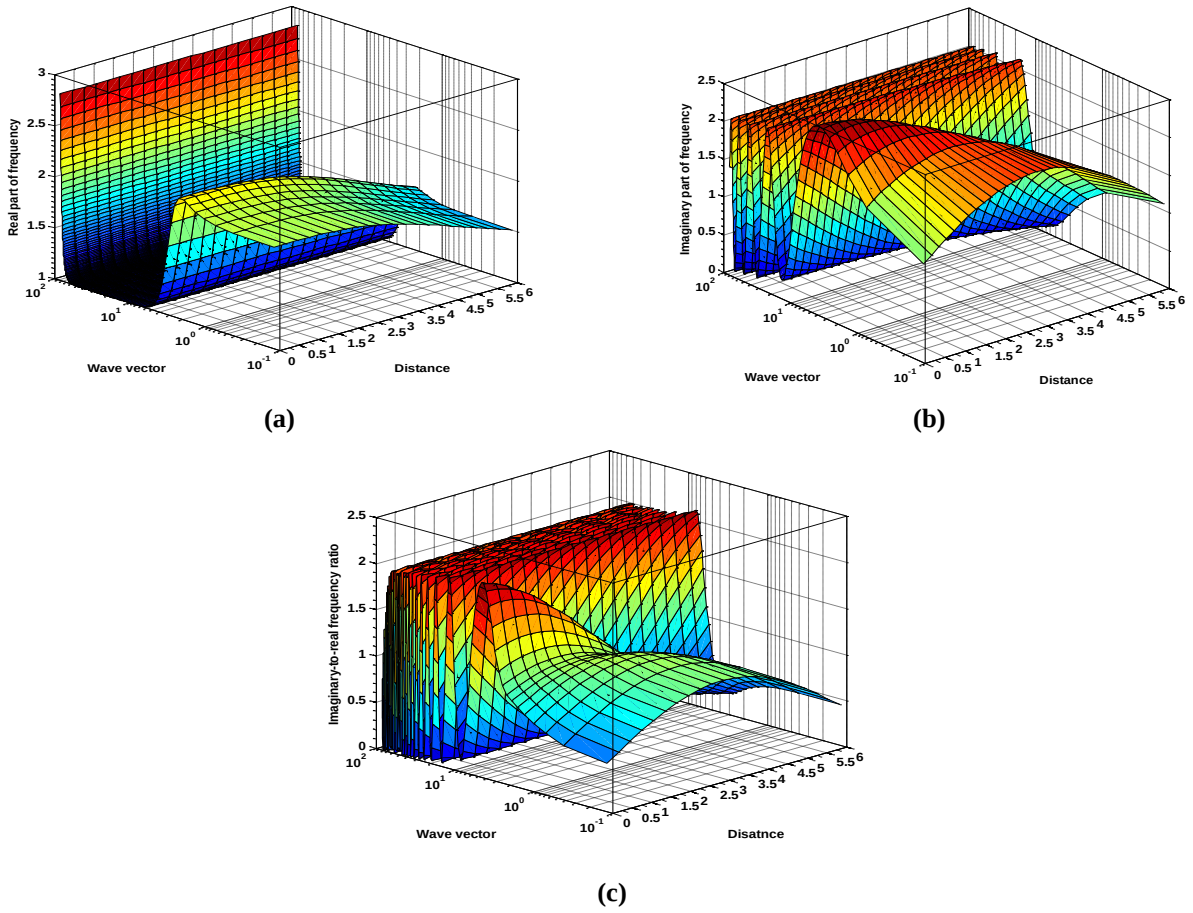

Figure 3.11 *Same as figure 3.9, but in the small-wavelength regime ($k \to \infty$).*

Figure 3.12 graphically presents the profile of normalized (a) phase velocity and (b) group velocity of the fluctuations with normalized distance (ξ) and normalized wave vector (k). The different input initial values used are the same as figure 3.8. In the ξ-space, the phase velocity (Figure 3.12(a)) shows a linearly damping behavior from the center outwards, due to decrease in the dust concentration. In the k-space, the phase velocity shows resonantly sharp decay from the center with a super-decay at $k = 1.5$ ($\lambda = 4.18\lambda_J$). After that, it shows slow variation. This shows that the Jeans mode dominates in the long-wavelength region and it is highly dispersive for the regime $k \le 1.5$. The group velocity profile shows that, the velocity of the Jeans mode wave amplitude is the maximum at the center and it linearly decreases outwards (Figure 3.12(b)). This signifies that the Jeans mode dominates in the CIP with the maximum value at the center. In the k -space, the group velocity shows a sharp damping from the center with a super-decay at $k = 1.5$ (

$\lambda = 4.18\lambda_J$). Again, after that, it grows linearly. Therefore, the group velocity shows dispersive nature of the fluctuations with mode-mode coupling characteristics of the wave-amplitude towards shorter-wavelengths via self-gravitational condensation of larger wavelengths.

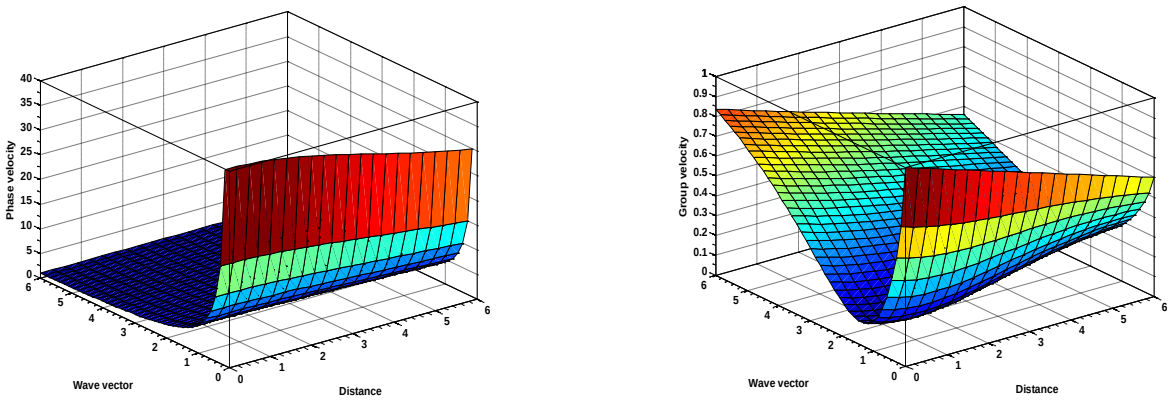

(a) **(b)**

Figure 3.12 *Profile of the normalized (a) phase velocity, and (b) group velocity of the fluctuations with normalized distance* (ξ) *and in normalized wave vector* (k). *The different input initial values used are the same as figure 3.8.*

Figure 3.13 shows the same as figure 3.7, but for the $\eta(\xi)$-fluctuations. It is seen that the real and imaginary parts of the fluctuation frequency decreases with increase in Z_d (Figure 3.13(a)) and increases with increase in m_d (Figure 3.13(b)). It is similar to figure 3.7, on the fact that for both the cases (Figures 3.13(a)-3.13(b)), the real part of frequency shows no variation in the regime $0 \le \xi \le 0.5\lambda_J$. The variation increases as the frequency shifts away from $\xi = 0.5\lambda_J$. The imaginary part reveals that, with increase in Z_d (Figure 3.13(a)), the growth rate remains the same in the CIP ($0 \le \xi \le 3.5\lambda_J$); but after CSB, it decreases with increase in Z_d. It is observed that, the growth rate increases from the center outwards with increase in m_d (Figure 3.13(b)). The electrostatic repulsive force in the cloud increases with increase in Z_d, which dominates the self-gravitational counterparts. Thus, the growth rate decreases with increase in Z_d in the CEP. Again, when m_d increases, the self-gravitational attractive force in the cloud increases, which increases the growth rate. From figure 3.13(a), the value of real and imaginary parts at the CSB are $(\omega_r)_G \sim 1.7$, and

$(\omega_i)_G \sim 2.0$, respectively. Similarly, from figure 3.13(b), one gets $(\omega_r)_G \sim 1.75$, and $(\omega_i)_G \sim 2.0$ at the CSB.

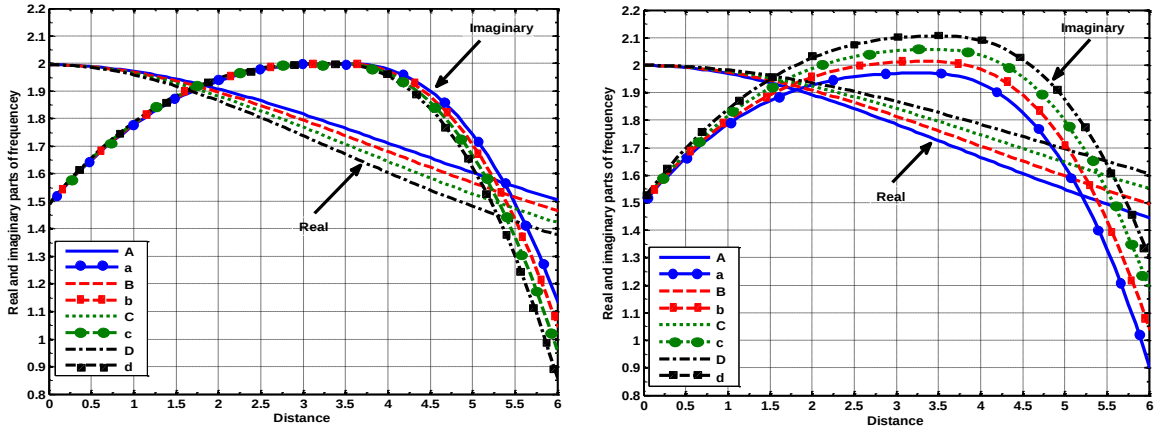

(a) **(b)**

Figure 3.13 *Same as figure 3.7, but now for the* $\eta(\xi)$*-fluctuations. The different input initial values used are the same as figure 3.8.*

Thus, it is confirmed that the CSB is most unstable electrostatic potential boundary, which is non-rigid in nature. In is also observed from figure 3.3(c), that the value of ratio of imaginary-to-real frequency at the CSB is $(\omega_i/\omega_r)_E \sim 1$, and its value for the self-gravitational counterpart from figure 3.9(d) is $(\omega_i/\omega_r)_G \sim 1.12$. The ratio of both the values is $R = (\omega_i/\omega_r)_E/(\omega_i/\omega_r)_G \sim 0.89$. At the CSB, from the frequency profiles, we get $(f_{Z_d})_r = (\omega_r)_E/(\omega_r)_G = 2.25/1.7 \sim 1.32$ (from figures 3.7(a), 3.13(a)), and $(f_{Z_d})_i = (\omega_i)_E/(\omega_i)_G = 2.25/2 \sim 1.12$ (from figure 3.7(a), 3.13(a)), for increasing grain-charge. Thus, at the CSB, the electrostatic instabilities are more dominant than the self-gravitational ones with increasing Z_d. Similarly, at CSB, we obtain $(f_{m_d})_r = (\omega_r)_E/(\omega_r)_G = 2.2/1.75 \sim 1.25$ (from figures 3.7(b), 3.13(b)), and $(f_{m_d})_i = (\omega_r)_E/(\omega_r)_G = 2.2/2 \sim 1.1$ (from figures 3.7(b), 3.13(b)), for increasing grain-mass. It implies that, at the CSB, the electrostatic instabilities dominate over the self-gravitational counterparts.

3.7 CONCLUSIONS

We present a self-consistent description of the nonlocal electro-gravitational instabilities supported in an inhomogeneous, non-uniform, self-gravitating charged DMC. We carry out a nonlocal linear

normal mode analysis to study the excitation and evolution characteristics of the fluctuations globally. We derive eigenvalue and eigen-function equations for the gravito-electrostatic fluctuations. A numerical scheme of realistic illustration is constructed with suitable initial input values. Based on the investigation, the following concluding remarks may be worth mentioning.

(1) An analytic non-local model to investigate the discrete behavior of the collective dynamics of global gravito-electrostatic fluctuations in spherical charged DMCs is developed.

(2) Eigenvalue and eigen-function equations are methodologically derived by applying the standard inhomogeneous Fourier technique exactly on the basis of plane wave analysis.

(3) The DMC is in unstable state, as the calculated mass ($M_D \sim 10^{21}$ kg) and scale-length ($R_D \sim 10^{11}$ m) of the DMC, are found greater than that of Avinash-Shukla critical mass limit ($M_D > M_{AS} \sim 10^{18}$ kg) and scale length ($R_D > L_{AS} \sim 10^{9}$ m) for astrophysical object to be in stable equilibrium state.

(4) Both electrostatic and self-gravitational potential fluctuations are found to be maximum at the CSB existing at $\xi = 3.5\lambda_J \sim 1.47 \times 10^{10}$ m with opposite polarity. This signifies that the CSB is the most unstable due to the strong coupling of the self-gravitational attractive and electrostatic repulsive effects contributed by the plasma species.

(5) Three distinct and spatio-spectrally isolated classes of nonlocal eigenmodes-dispersive, non-dispersive and hybrid types-are identified and characterized in detail.

(6) Dispersive features are prominent in the ultra-high *k*-regime; and non-dispersive characteristics dominate in the ultra-low *k*-regime.

(7) The ratio of electrostatic-to-self-gravitational potential fluctuations comes out as $\tilde{\theta}_1/\tilde{\eta}_1 \sim 7 \times 10^1$. This shows that, in our model, the strength of self-gravitational potential fluctuations is much smaller than that of the electrostatic counterpart.

(8) The density inhomogeneity, self-gravity and non-local wave characterization give rise to unique type of hybrid instability due to mode-mode coupling of electro-gravitational fluctuations. These type of instabilities may be responsible for the formation of stars and other astrophysical objects [35].

(9) The entire DMC is a mixture of both the Jeans and electrostatic modes. Near the center, the Jeans mode plays the dominating role, and away from it, the electrostatic mode prevails.

(10) The growth rate of the $\theta(\xi)$-fluctuations increases and $\eta(\xi)$-fluctuations decreases with the increase in the electrical charge of the massive dust grains. Moreover, the growth rate shows reverse characteristics with the increase in mass of the massive dust grains.

(11) Grain-charge has destabilizing influential role for the electrostatic fluctuations; but stabilizing role for the self-gravitational ones. Grain-mass plays stabilizing influential role for the electrostatic fluctuations; but destabilizing role for the self-gravitational ones.

(12) The present investigation may be useful for understanding the propagation of electro-gravitational waves and associated instabilities in interstellar dense DMCs and astrophysical plasmas, which contain a significant fraction of neutral atoms, and which are subjected to the self-gravitational force. The nonlocal instability evolution discussed here could be responsible for the fragmentation of molecular clouds into substructures, which in turn, may fail to be supported against the self-gravity and may collapse to form the stars in galaxies.

(13) Lastly, our nonlocal model analysis may provide extensive inputs for further study of excitation and evolution of different waves and instabilities of other realistic astrophysical objects, associated with dust charge fluctuations, collisions, etc. Further refinements with inclusion of neutral particle dynamics, grain charge fluctuations and non-static rotational behaviors associated with the cloud are being made in our future investigations.

REFERENCES

1. Bally, J. and Harrison, E.R. The electrically polarized universe, *ApJ* **220**, 743-744, 1978.
2. Vranjes, J. and Tanakaa, M. Y. On Gravity Induced Electric Field in Space Plasmas, *Phys. Scr.* **71**, 325-328, 2005.
3. Verheest, F. Waves and instabilities in dusty space plasmas, *Space Sci. Rev.* **77**, 267-302, 1996.
4. Verheest, F. *Waves in Dusty Space Plasmas*, Kluwer Academic Publisher, Netherlands, 2000.
5. Shukla, P. K. and Mamun, A. A. Fragmentation instability of molecular clouds, *Phys. Lett. A* 271, 402-406, 2000.
6. Mamun, A. A. and Shukla, P. K. Instabilities in a nonuniform partially ionized isothermal magnetoplasma, ApJ, 548, 269-277, 2001.
7. Spitzer, L., Jr. *Physical Processes in the Interstellar Medium*, WILEY-VCH Verlag GmbH & Co. KGaA, Weinheim, 2004.

8. Tielens, A. G. G. M. & Allamandola, L. J. Evolution of interstellar dust, in *Physical Processes in Interstellar Clouds*, G. E. Morfill et al., eds., Reidel Publishing Company, Holland, 1987, 333-376.
9. Hoyle, F. & Wickramasinghe, N. C. *The Theory of Cosmic Grains*, Springer, Dordrecht, 1991.
10. Vaisberg, O. L., et al. Spatial and mass distribution of low-mass dust particles ($m < 10^{-10}$ g) in comets P/Halley's coma, *A&A* **187**, 753-760, 1987.
11. Friberg. P., and Hajalmarson, A. Molecular clouds in the Milky Way, in *Molecular Astrophysics*, T. W. Hartquist, ed., Cambridge University Press, New York, 1990, 3-34.
12. Kutner, M. L. *Astronomy: A Physical Perspective*, Cambridge University Press, New York, 2003.
13. Stahler, S. W. & Palla, F. *The Formation of Stars*, WILEY-VCH Verlag GmbH & Co. KGaA, Weinheim, 2004.
14. Peratt, A. L. *Physics of the Plasma Universe*, 2nd ed., Springer, New York, 2015.
15. Jeans, J. H. The stability of a spherical nebula, *Phil. Trans. Roy. Soc*. **199,** 1-53, 1902.
16. Chandrasekhar, S. *An Introduction to the Study of Stellar Structure*, Dover, New York, 1957.
17. Pudritz, R. E. The stability of molecular clouds, *ApJ* **350**, 195-208, 1990.
18. Mamun, A. A., et al. Ultra-low-frequency electrostatic waves in a self-gravitating magnetized and inhomogeneous dusty plasma, *Planet. Space Sci.* **47**, 79-83, 1999.
19. Mamun, A. A. and Shukla, P. K. Instabilities of self-gravitating dusty clouds in magnetized plasmas, Phys. Plasmas, 7, 3762-3770, 2000.
20. Avinash, K. and Shukla, P. K. A purely growing instability in a gravitating dusty plasma, *Phys. Lett. A* **189**, 470-472, 1994.
21. Pandey, B. P., et al. Jeans instability of a dusty plasma, *Phys. Rev. E* **49**, 5599-5606, 1994,
22. Verheest, F., et al. Jeans instability in partially ionized self-gravitating dusty plasmas, *Phys. Rev. E* **68**, 027402 (1)-027402(4), 2003.
23. Rao, N. N., et al. Dust-acoustic waves in dusty plasmas, *Planet. Space Sci.* **38**, 543-546, 1990.
24. Avinash, K. and Shukla, P. K. Gravitational equilibrium and the mass limit for dust clouds, *New J. Phys*. **8**, 2(1)-2(10), 2006.
25. Pandey, B. P., et al. Equilibrium properties of a gravitating dusty plasma, *Phys. Scr*. **66**, 269-272, 2002.

26. Karmakar, P. K. A new technique for electromagnetic characterization of spherical dust molecular cloud equilibrium structure, *Results in Physics* **2**, 77-89, 2012.
27. Borah, B. and Karmakar, P. K. A theoretical model for electromagnetic characterization of a spherical dust molecular cloud equilibrium structure, *New Astronomy* **40**, 49-63, 2015.
28. Melrose, D. B. *Instabilities in Space and Laboratory Plasmas*, Cambridge University Press, New York, 1986.
29. Carbonell, M., et al. Time damping of linear non-adiabatic magnetohydrodynamic waves in an unbounded plasma with solar coronal properties, *A&A* **415**, 739-750, 2004.
30. Cattaert,T. and Verheest, F. Solitary waves in self-gravitating molecular clouds, *A&A* **438**, 23-29, 2005.
31. Chen, C.-L. *Foundations for Guided-Wave Optics*, John Wiley & Sons, New Jersey, 2007.
32. Nishikawa, K. & Wakatani, M. *Plasma Physics: Basic Theory with Fusion Applications*, Springer, Berlin, 1990.
33. Otto, S. R. & Denier, J. P. *An Introduction to Programming and Numerical Methods in MATLAB*, Springer, London, 2005.
34. Shadmehri, M. and Dib, S. Magnetothermal condensation modes including the effects of charged dust particles, *MNRAS* **395**, 985-990, 2009.
35. Vranjes, J. Gravitational instability of a quasi-homogeneous plasma cloud with radiation, *Astrophys. Space Sci.* **173**, 293-298, 1990.